# 2024-2025

# Cornell NanoScale Facility (CNF)

# RESEARCH ACCOMPLISHMENTS

# **Tunable Elliptical Cylinders for Rotational Mechanical Studies of Single DNA Molecules**

**CNF Project Number: 1738-08** 

Principal Investigator(s): Michelle D. Wang

**User(s): Yifeng Hong** 

Affiliation(s): Department of Electrical and Computer Engineering, Cornell University, Department of Physics, Cornell University, Howard Hughes Medical Institute

Primary Source(s) of Research Funding: Howard Hughes Medical Institute

Contact: mdw17@cornell.edu, yh874@cornell.edu

Research Group Website: http://wanglab.lassp.cornell.edu/

Primary CNF Tools Used: ASML DUV Stepper, Oxford 81 Etcher, Oxford 82 Etcher, Oxford PECVD, SC4500 Odd-Hour Evaporator, CVC SC4500 Evaporators, Zeiss Supra SEM, Zeiss Ultra SEM

#### **Abstract:**

The angular optical trap (AOT) is a powerful technique for measuring the DNA topology and rotational mechanics of fundamental biological processes. Realizing the full potential of the AOT requires rapid torsional control of these processes. However, existing AOT quartz cylinders are limited in their ability to meet the high rotation rate requirement while minimizing laser-induced photodamage. In this work, we present a trapping particle design to meet this challenge by creating small metamaterial elliptical cylinders with tunable trapping force and torque properties. The optical torque of these cylinders arises from their shape anisotropy, with their optical properties tuned via multilayered SiO2 and Si3N4 deposition. We demonstrate that these cylinders can be rotated at about three times the rate of quartz cylinders without slippage while enhancing the torque measurement resolution during DNA torsional elasticity studies. This approach opens opportunities for previously inaccessible rotational studies of DNA processing.

## **Summary of Research:**

We have achieved our goal by creating smaller elliptical cylinders with tunable trapping force and torque properties<sup>1</sup>. Instead of using optical birefringence for optical torque generation as with the quartz cylinders, these elliptical cylinders experience an optical torque via their shape anisotropy because the major axis of their elliptical cross-section tends to align with the laser's linear polarization (Fig. 1, A and B). These cylinders are made of a metamaterial that affords an effective index of refraction higher than quartz via alternating layers of SiO2 and Si3N4 (Fig. 1C).

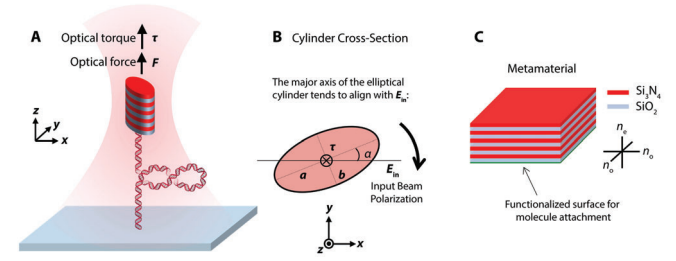


Figure 1: Operational principle of a metamaterial elliptical cylinder in an AOT. (A) experimental configuration of DNA torsional mechanics measurements using a meta-material elliptical cylinder in an AOT. (B) Optical torque generation of a dielectric elliptical cylinder. (C) The metamaterial.

We optimized the optical force, torque, and trapping stability by tuning the size, shape, and composition of these particles via an established COMSOL simulation platform<sup>1,2</sup>. Then, we nanofabricated the metamaterial elliptical cylinders with the targeted dimensions obtained from simulations via a top-down, DUV lithography-based process (Fig. 2A). The liftoff method for cylinder collection resulted in more uniform metamaterial elliptical cylinders with ~ 4-times volume

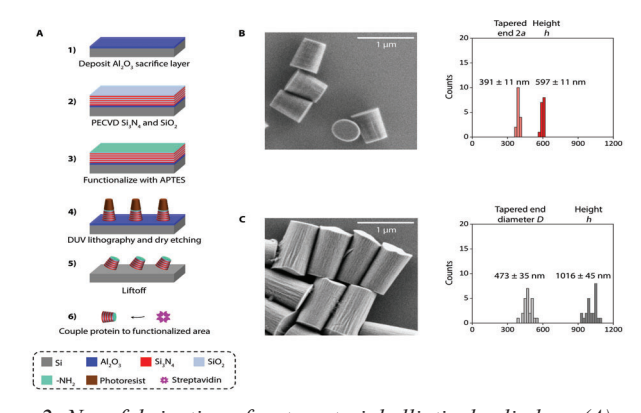


Figure 2: Nanofabrication of metamaterial elliptical cylinders. (A) Fabrication process flow of metamaterial elliptical cylinders. (B) An SEM image of nanofabricated metamaterial elliptical cylinders. The size and uniformity characterization is also shown. (C) An SEM image of nanofabricated quartz cylinders. The size and uniformity characterization is also shown.

reduction compared with the conventional quartz cylinders (Fig. 2, B and C).

We validated the trapping properties of these nanofabricated metamaterial elliptical cylinders with the AOT. We showed that our metamaterial elliptical cylinders can generate a maximum force and a maximum torque comparable to the quartz cylinders (Fig. 3, A and B). In addition, we measured the rotational motion of metamaterial elliptical cylinders and found they show a threefold reduction in  $\gamma\theta$ :  $3.2 \pm 0.3$  pN·nm·s/turn (mean  $\pm$  SD, n = 17), in comparison to  $9.4 \pm 1.7$  pN·nm·s/turn (mean  $\pm$  SD, n = 14) of the quartz cylinder (Fig. 3A). The reduced  $\gamma\theta$  of the metamaterial elliptical cylinders resulted in  $\sim$  3- times faster cylinder rotation rate without slippage (Fig. 3B).

Moreover, the reduced  $\gamma_\theta$  of the metamaterial elliptical cylinders also had an extra benefit of a greater signal-to-noise ratio (SNR) in the torque measurement of a DNA molecule. This threefold reduction in  $\gamma\theta$  should provide a 1.7-fold reduction in the noise of the measured torque of a DNA molecule, which was experimentally validated via the DNA torsional measurements (Fig. 4, A, B, and C).

## **Conclusions and Future Steps:**

We demonstrated, both theoretically and experimentally, that our small-size biocompatible metamaterial elliptical cylinders can permit cylinder rotation about three times the rate of the quartz cylinders while providing high force and torque for DNA torsional mechanics studies with enhanced torque resolution. Moreover, our methodology offers versatility in tuning the refractive index, shape anisotropy, and cylinder size to optimize the trapping properties. We anticipate that using these cylinders can enable previously inaccessible rotational studies of DNA-based biological processes.

#### **References:**

- [1] Hong, Y.; Ye, F.; Gao, X.; Inman, J. T.; Wang, M. D. Tunable Elliptical Cylinders for Rotational Mechanical Studies of Single DNA Molecules. Sci. Adv. 10 (50), eadr4519. 2024 https://doi.org/10.1126/sciadv.adr4519.
- [2] Hong, Y.; Ye, F.; Qian, J.; Gao, X.; Inman, J. T.; Wang, M. D. Optical Torque Calculations and Measurements for DNA Torsional Studies. Biophys. J. 2024. https://doi.org/10.1016/j. bpj.2024.07.005.

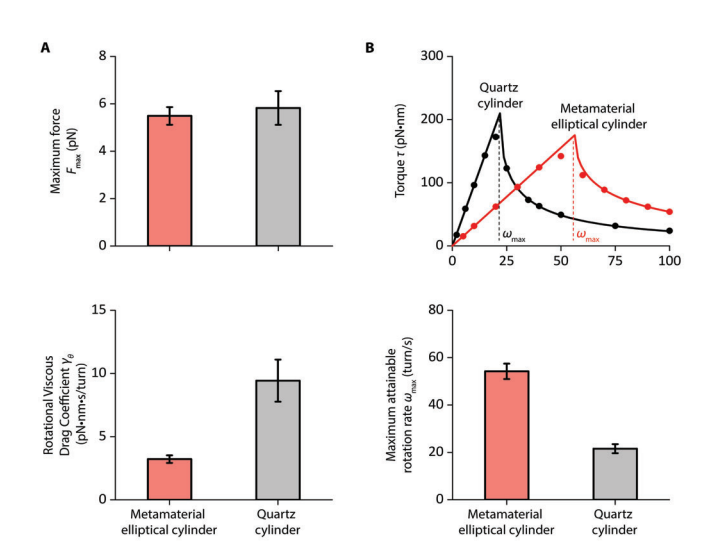


Figure 3: Trapping properties and maximum rotation rate of metamaterial elliptical cylinders. (A) Measurements of the maximum trapping force Fmax (top panel) at 30 mW laser power before the objective and rotational viscous drag coefficient  $\gamma\theta$  (bottom panel). (B) Method to determine the

maximum trapping torque \tau (top panel) and the maximum rotation rate \text{omax} (bottom panel) without slippage at 30 mW laser power before the objective.

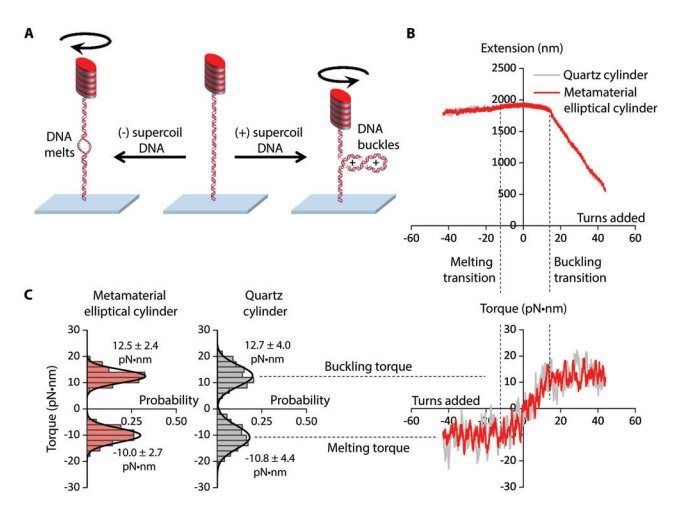


Figure 4: DNA torque measurements using a metamaterial elliptical cylinder, in comparison with those from a quartz cylinder. (A) experimental configuration for the measurements. (B) Measured DNA extension and torque as a function of turns added to DNA under 1 pN force. (C) Histograms of measured torque upon (+) DNA buckling and (-) DNA melting. Each histogram is fit by a Gaussian, with the mean and the SD of the fit shown.

# Building Microfluidics Devices to Study Zinc Metal Homeostasis in E. Coli Communities

**CNF Project Number: 1844-09** 

Principal Investigator(s): Peng Chen

**User(s): Felix Alfonso** 

Affiliation(s): Department of Chemistry and Chemical Biology, Cornell University

Primary Source(s) of Research Funding: National institute of health and the national institute of general medical

sciences

Contact: pc252@cornell.edu, fsa33@cornell.edu

Research Group Website: http://chen.chem.cornell.edu/

Primary CNF Tools Used: Heidelberg DWL2000 Mark Writer, SUSS MA6-BA6 Contact Aligner, Oxford Cobra ICP

Etcher, Plasma-Therm Deep Silicon Etcher, and P7 Profilometer

#### **Abstract:**

Bacterial organisms have developed sophisticated biochemical mechanisms to absorb vital nutrients from their surroundings while expelling surplus materials to avoid toxic accumulation. This research seeks to understand how single microbial units contribute to maintaining metal equilibrium within larger bacterial populations. To accomplish this objective, we created a specialized microfluidic system that enables precise cultivation of Escherichia coli colonies in carefully designed microscopic compartments. The size of these compartments was deliberately calibrated to match E. coli cell dimensions, creating controlled spatial restrictions that serve as a fundamental component of the experimental approach. The microfluidic platforms utilized in this work provide sophisticated environmental regulation capabilities, offering exceptional opportunities to examine and comprehend microbial behavior. Through this technology, we could examine in detail how these microscopic bacterial communities maintain equilibrium in their zinc metabolism processes. We utilized cutting-edge genetic engineering methods to develop E. coli variants containing luminescent protein indicators. This specialized genetic alteration enabled the observation and measurement of the activity of genes associated with complex ion transport systems, particularly focusing on zinc-specific pathways. The findings from this investigation may significantly advance our comprehension of microbial communities and their environmental relationships.

# **Summary of Research:**

As an essential trace element, zinc plays a critical role in the survival of all life forms (1). This micronutrient

performs crucial tasks in enzymatic processes, protein structure formation, and transcriptional control (2,3). When zinc concentrations become unbalanced significant disruptions occur in intestinal microbial communities, leading to detrimental health outcomes (4, 5). Throughout evolutionary history, microorganisms have evolved sophisticated molecular systems that enable efficient nutrient uptake from their surroundings while simultaneously expelling surplus amounts to avoid cellular damage. Bacterial cells control these export mechanisms by regulating the production of transport proteins through metal-sensitive transcriptional controllers. These regulatory elements monitor intracellular metal ion concentrations, directing cellular processes toward optimal metal balance. This research aims to investigate and measure zinc ion (Zn<sup>2+</sup>) management within microbial communities, illuminating how single bacterial cells contribute to maintaining metal equilibrium across entire populations. We selected Escherichia coli as our experimental model to examine the intricate mechanisms of communitybased zinc regulation. The inherent mobility of E. coli and its weak surface adhesion properties create obstacles for extended microscopic observation studies. Nevertheless, microfluidic technology provides an elegant solution by creating controlled experimental conditions suitable for bacterial community research (6). These microfluidic systems enable precise regulation of nutrient delivery and have proven successful in longterm imaging investigations (7).

Our experimental microfluidic apparatus incorporates two essential elements: flow channels, and microscopic cultivation chambers. The depth of these cultivation chambers is specifically designed to correspond with E. coli cell diameter (approximately 1 micrometer), enabling effective bacterial colony containment.

In Figure 1, we can observe a single layer of E. coli cultivated under 10 micromolar zinc conditions. The red marking indicates the chamber boundary, within which support pillars are positioned to prevent structural collapse while serving as reference points for distance

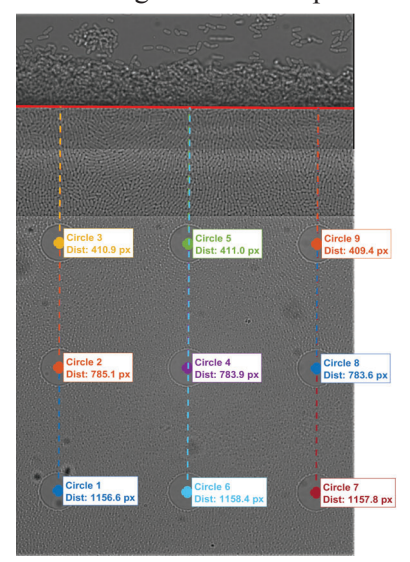


Figure 1: Monolayer of E. coli cells grown in microfluidic microchamber under 10 micromolar zinc exposure. The red line indicates the beginning of the chamber. Support posts within the chamber prevent ceiling collapse and serve as fiducial markers for distance calibration.

measurements from the pillar to the chamber opening. Through time-lapse fluorescence microscopy, we can monitor the activation of the ZntA efflux protein during continuous exposure to 10 micromolar zinc concentration. The resulting curve displays initial S-shaped kinetics followed by sharp increases in later time periods (Figure 2). By utilizing spatial coordinates from the reference markers, we can organize our data according to distance from the channel entrance, providing insights into how gene expression varies with spatial position. This visualization is achieved through a two-dimensional histogram plotting distance (y-axis) versus time (x-axis) with concentration values as binned data (Figure 3). This microfluidic platform enables comprehensive spatial-temporal analysis of efflux protein and channel gene expression, potentially establishing a foundation for understanding metal homeostasis mechanisms and developing therapeutic strategies that target bacterial metal regulation systems.

Microfluidic device fabrication uses standard silicon nanofabrication. Silicon wafers are cleaned with piranha solution, coated with photoresist, and patterned using a custom photomask and Karl SUSS MA6-BA6 Contact aligner. Chambers are etched ~1µm deep using Oxford Cobra ICP Etcher. Channels are formed via SU-8 photolithography, cured at 95°C, then hard baked

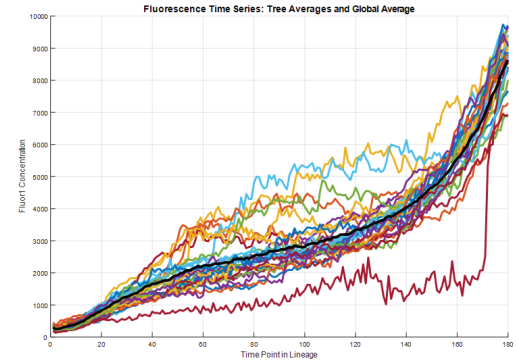


Figure 2: Time-course induction of ZntA efflux protein (nanomolar) expression under constant 10 micromolar zinc exposure measured by time-lapse fluorescent microscopy.

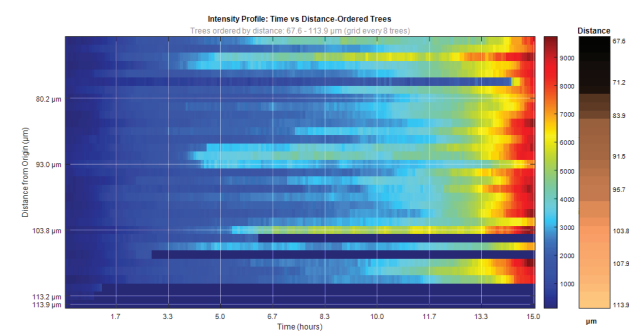


Figure 3: Two-dimensional histogram showing ZntA protein concentration (nanomolar) as a function of distance from channel entrance (y-axis) and time (x-axis).

at 200°C for 10 minutes. The silicon template is coated with FOTS for easy PDMS removal. Completed devices are bonded to coverslips, loaded with bacterial cells, and imaged using appropriate microscopy equipment.

- [1] R. R. Robert B. Saper, Zinc: An Essential Micronutrient. Am. Fam. Physician. 79, 768 (2009).
- [2] S. Tan, D. Guschin, A. Davalos, Y.-L. Lee, A. W. Snowden, Y. Jouvenot, H. S. Zhang, K. Howes, A. R. McNamara, A. Lai, C. Ullman, L. Reynolds, M. Moore, M. Isalan, L.-P. Berg, B. Campos, H. Qi, S. K. Spratt, C. C. Case, C. O. Pabo, J. Campisi, P. D. Gregory, Zinc-finger protein-targeted gene regulation: genomewide single-gene specificity. Proc. Natl. Acad. Sci. U. S. A. 100, 11997–12002 (2003).
- [3] C. Andreini, I. Bertini, in Encyclopedia of Metalloproteins (Springer, New York, NY, 2013), pp. 2549–2554.
- [4] S. R. Gordon, S. Vaishnava, Zinc supplementation modulates T helper 17 cells via its effect on gut microbiome. The Journal of Immunology. 204, 83.18–83.18 (2020).
- [5] O. Koren, E. Tako, Chronic Dietary Zinc Deficiency Alters Gut Microbiota Composition and Function. Proc.AMIA Annu. Fall Symp. 61, 16 (2020).
- [6] F. Wu, C. Dekker, Nanofabricated structures and microfluidic devices for bacteria: from techniques to biology. Chem. Soc. Rev. 45, 268–280 (2016).
- [7] D. Binder, C. Probst, A. Grünberger, F. Hilgers, A. Loeschcke, K.-E. Jaeger, D. Kohlheyer, T. Drepper, Comparative Single-Cell Analysis of Different E. coli Expression Systems during Microfluidic Cultivation, PLoS One. 11, e0160711 (2016).

# Microfabricated Nanogrooves to Promote in Vitro Muscle Fiber Differentiation and Maturation

**CNF Project Number: 2065-11** 

Principal Investigator(s): Jan Lammerding User(s): Eitan Jentis, Maggie Elpers, Sarah Henretta, Anna Hazelwood

Affiliation(s): Meinig School of Biomedical Engineering, Weill Institute for Cell and Molecular Biology, Cornell University

Primary Source(s) of Research Funding: National Institutes of Health award R01 HL082792; National Institutes of Health award R01AR084664

Contact: ej225@cornell.edu, mae228@cornell.edu, sjh333@cornell.edu, alh333@cornell.edu

Research Group Website: http://lammerding.wicmb.cornell.edu/

Primary CNF Tools Used: Plasma-Therm Unaxis DRIE, Oxford Cobra etcher, Heidelberg DWL 2000 Mask Writer, GCA AS200 i-line Stepper, Karl Suss MA6 Contact Aligner, Anatech SCE-110-RF Resist Stripper, P-7 Profilometer, MVD-100; Oxford 81 etcher; Unaxis 770 Deep Silicon Etcher; BLE150 Hotplate; EcoClean Asher; PDMS spin coater

#### **Abstract:**

Muscular dystrophy encompasses a group of devastating diseases affecting skeletal muscle in young children and resulting in reduced mobility and premature death. Gaining a better understanding of the underlying disease mechanism is crucial for developing effective therapies, which are currently lacking. One challenge in studying the pathogenesis of muscular dystrophies is that common in vitro models based on the differentiation of skeletal muscle stem cells (myoblasts) do not match the form and function of skeletal muscle tissue in vivo, including the highly aligned and organized muscle fibers. Culturing myoblasts on nanostructured surfaces that provide physical cues for the differentiating muscle cells has been shown previously to promote the formation of mature and highly aligned muscle fibers. Here, we demonstrate the use of microfabricated silicon wafers that serve as molds to generate polydimethylsiloxane (PDMS) membranes with ~700 nm wide and ~1300 nm deep nanogrooves. These PDMS substrates, when coated with Matrigel extracellular matrix, enable the differentiation of primary mouse myoblasts into mature and well-aligned skeletal muscle fibers, which we are now using as a model system to study Emery-Dreifuss muscular dystrophy and other muscle diseases caused by mutations in the LMNA gene.

# **Summary of Research:**

Mutations in the LMNA gene, which encodes the nuclear envelope proteins lamin A and C (lamin A/C), cause Emery-Dreifuss muscular dystrophy, congenital muscular dystrophy, and dilated cardiomyopathy. Although lamin A/C is expressed in nearly every

tissue, most LMNA mutations primarily affect striated muscle, i.e., skeletal and cardiac muscle. Both the molecular mechanism underlying the muscle-specific defects and the pathobiology of the disease remain incompletely understood, presenting a major obstacle in the development of effective therapies. While animal models for these diseases are available, they are limited in their ability to allow detailed cell and molecular level observations of the disease progression, which is required to identify pathogenic mechanisms. In vitro models, on the other hand, are well suited for imaging but do not capture the structure and function of mature muscle tissue, limiting their usefulness. To overcome this challenge, we developed PDMS-based in vitro cell culture substrates with nanostructured ridges that are ~700 nm wide, ~1300 nm tall, and separated by ~700 nm wide gaps, to resemble in vivo tissue architecture and promote muscle cell differentiation and alignment.

We first fabricate silicon wafers to serve as molds to cast the nanostructured PDMS substrates (Figure 1). Oir620-7i photoresist is spin-coated onto a 4-inch wafer and exposed to UV light using the GCA AS200 i-line stepper to imprint the pattern into the photoresist layer. After developing the photoresists using the 726 MIF, we perform a silicon etch with the Unaxis 770 Deep Silicon Etcher, removing silicon in the regions not covered by photoresist. After etching, the remaining photoresist is stripped, and a hydrophobic Teflon coating is applied to the wafer to prevent PDMS from sticking, thus making the wafer suitable as a mold to cast thin sheets of PDMS containing the desired nanostructures. We confirmed the desired dimensions of the ridges on the silicon wafer using the Zygo Optical Profiler and scanning electron microscopy (Figure 2). Subsequently, PDMS is spincoated onto the silicon wafer and cured by baking for >2 hours at 60°C. The PDMS sheets are then removed from the wafer and coated with Matrigel, an extracellular matrix molecule that supports muscle cells in vivo. Primary mouse myoblasts are cultured on the nanostructured PDMS substrate and induced to differentiate into muscle fibers, starting one day after plating. We use an Airyscan LSM900 confocal microscope to observe the cells and assess their alignment and maturity based on their sarcomeric structures. Figure 3 shows a representative image of wild-type muscle cells differentiated into >400 µm long muscle fibers with the characteristic striated sarcomere patterning and high alignment between muscle fibers.

Having established this experimental platform, we are now using it to compare LMNA mutant and wild-type muscle cells and determine the molecular mechanism responsible for the muscle defects. In addition to promoting muscle differentiation and alignment, the flexible PDMS substrate also enables us to apply mechanical strain to the muscle fibers, allowing us to test the hypothesis that the LMNA mutant muscle cells are more sensitive to mechanical stress, which could explain the muscle-specific defects of many laminopathies.

Taken together, this application illustrates new uses of the available nanofabrication technologies to create improved in vitro models to study normal muscle differentiation and muscle disease.

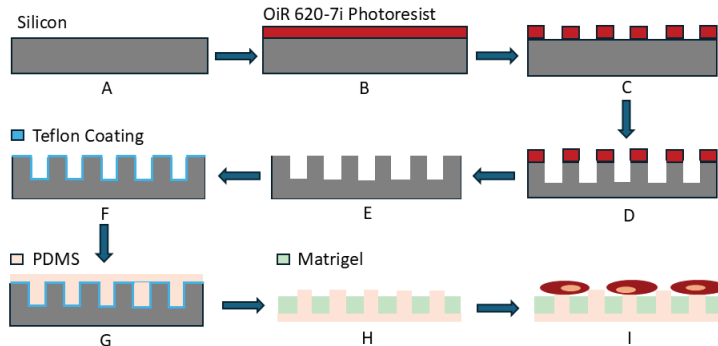


Figure 1: Nanofabrication process for nanostructured surfaces. A 4-inch n-type silicon wafer (A) is spin coated with OiR620-7i photoresist to 0.72 µm thickness (B), followed by exposure and development of the photoresist using the AutoStep 200 DSW i-line Stepper to create the desired patterns (C), which are then etched 1.3 µm deep into the silicon wafer using the Unaxis 770 system (D). After stripping the photoresist (E), a thin Teflon coating is applied (F) to prevent PDMS from sticking when cast onto the wafer (G). After removal of the PDMS substrate from the wafer, extracellular matrix, Matrigel, is applied to the wafer (H). Finally, primary muscle stem cells (myoblasts) are cultured on the substrate (I) and induced to differentiate into skeletal muscle fibers.

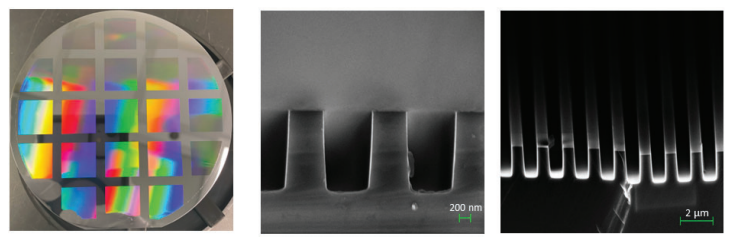


Figure 2: Characterization of the nanostructured silicon wafer. Photograph of the final wafer, with arrays of 1 cm  $\times$  1 cm squares containing the nanostructured ridges visible (left). Scanning electron microscope (SEM) images of the cross-section of the wafer are shown at high (center, scale bar = 200 nm) and low resolution (right, scale bar = 2  $\mu$ m). The width of each ridge is around 660 nm, and the depth is 1.3  $\mu$ m. The SEM images were taken on the Zeiss Ultra SEM.

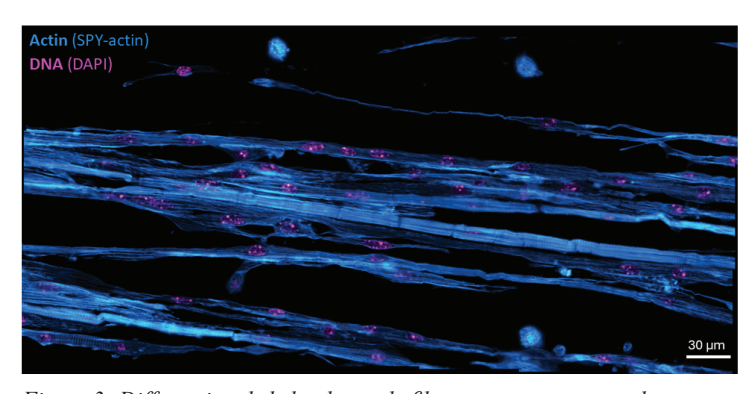


Figure 3: Differentiated skeletal muscle fibers on nanostructured substrate. Fluorescence microscopy image of primary mouse myoblast differentiated into muscle fibers and stained for DNA (DAPI) and actin (SPY-actin 555) to visualize sarcomeres, the contractile units of striated muscle.

# Microfluidic Flow Cells for Time-Resolved Fluorescence-Based Studies of Biomolecules

**CNF Project Number: 2158-12** 

Principal Investigator(s): Lois Pollack

**User(s): Scout Fronhofer** 

Affiliation(s): Cornell University, Applied and Engineering Physics Primary Source(s) of Research Funding: National Institutes of Health

Contact: lp26@cornell.edu, shf56@cornell.edu

Research Group Website: https://pollack.research.engineering.cornell.edu/

Primary CNF Tools Used: Heidelberg DWL2000, Oxford PECVD, ABM mask aligner, Oxford 80 RIE, Unaxis 770 Deep

Silicon Etch, Suss SB8e Substrate Bonder, DISCO dicing Saw

#### **Abstract:**

We report the fabrication of microfluidic flow cells for time-resolved fluorescence measurements of biological molecules. These silicon and glass devices improve upon our previous design by allowing the CNF-fabricated flow cell to be combined with multiple types of microfluidic mixers. The simplified design will enable time-resolved studies of interactions between biological molecules such as nucleic acids and proteins.

## **Summary of Research:**

Single-molecule fluorescence techniques are useful tools for studying dynamic, flexible biological molecules including single-stranded nucleic acids. One such method is fluorescence correlation spectroscopy (FCS) which can provide information about the size and interactions of molecules in solution by measuring the fluctuations in emitted photons from fluorescently labeled molecules in solution as they diffuse in and out of a laser confocal volume [1]. Another useful technique is Förster resonance energy transfer (FRET), which takes advantage of the distance dependence of energy transfer between pairs of fluorescent dyes to measure inter- and intra-molecular distances. At the single molecule level, these measurements provide insight into the dynamics and distribution of conformations in heterogeneous samples such as disordered single-stranded RNA [2]. Microfluidic devices enable time-resolved versions of these experiments, where a biological interaction is initiated and probed as a function of time as the molecules flow along a channel.

Here we describe the fabrication of durable, reusable microfluidic channels that can interface with our lab-built confocal fluorescence microscope as well as different types of microfluidic mixers, providing flexibility in terms of the techniques we can use and the biological

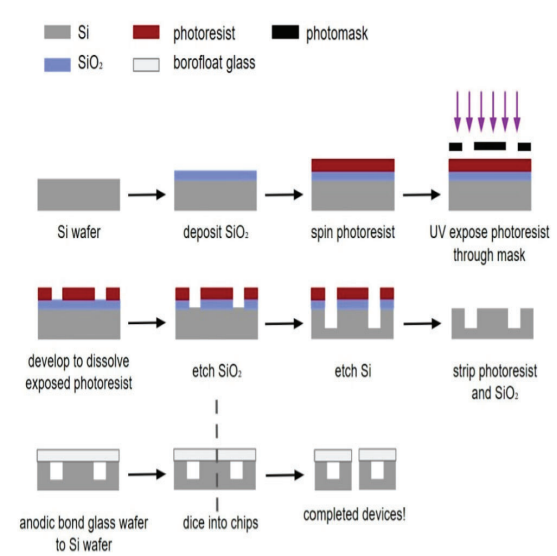


Figure 1: Fabrication process for making many silicon and glass flow cells out of a single wafer.

systems we can investigate. The design is based on our previously established protocol for fabricating mixing devices microfluidic for time-resolved fluorescence measurements [3]. We now improve upon the earlier design by fabricating a simplified flow cell which can be interfaced with different microfluidic mixers depending on the properties of the system being studied. The flow cell consists of a channel etched into silicon, sealed by borofloat glass to make it compatible with a water immersion objective lens. The fabrication process, outlined in Figure 1, consists of several steps making use of the photolithography, etching, and bonding tools at the CNF. First, a layer of silicon dioxide is deposited onto a silicon wafer using the Oxford PECVD tool. This oxide layer serves as a hard mask for deep etching of the silicon. Next, a layer of photoresist is spun and baked onto the wafer before being exposed through a mask using the ABM contact aligner. After developing to remove the exposed photoresist, we etch



Figure 2: The image on the left shows several flow cells at the end of the fabrication process, after the bonded silicon and glass wafers have been diced. The image on the right is a stereoscope view of one flow cell, with a square opening at the front and the channel visible through the layer of glass.

first through the oxide using the Oxford 81/82, then into the silicon using the Unaxis deep silicon etcher, creating channels that are 200  $\mu m$  wide and 200  $\mu m$  deep. To seal the top of the channels, a 200 $\mu m$  thick borofloat glass wafer is anodically bonded to the silicon using the Suss SB8E substrate bonder. Finally, the bonded wafers are diced into 1 cm x 1 cm chips. One wafer processed in this way results in about 40 individual chips, each of which contains a 200  $\mu m$  x 200  $\mu m$  square channel, sealed on four sides and open on the ends to allow for flow through the channel. A diced wafer and an individual chip are shown in Figure 2.

The completed chips, or flow cells, can then be coupled with a microfluidic mixer to perform time-resolved experiments. The simplicity of the design means that the mixer upstream of the flow cell can be customized for each experiment. Depending on the sizes of the biological molecules being mixed and the timescales of interest, a suitable mixer can be built to efficiently mix the reactant molecules and flow them through the observation channel where fluorescence measurements are recorded. For example, a system in which a small molecule is reacting with a large molecule might employ a coaxial diffusive mixer, while fast mixing of two large molecules requires a different method of mixing such as chaotic advection in a 3D printed mixer [4].

## **Conclusions and Future Steps:**

We have fabricated versatile flow cells which, when paired with microfluidic mixers, will allow us to use time-resolved fluorescence techniques to study a variety of dynamic biological molecules. Future experiments will use these devices to investigate systems such as nucleic acid-protein and nucleic acid-nucleic acid interactions. These experiments will complement the structural information that can be obtained from other techniques, particularly x-ray scattering.

- [1] Elson, Elliot L. "Fluorescence correlation spectroscopy: past, present, future." Biophysical journal 101.12 (2011): 2855-2870
- [2] Wang, Tong, et al. "Sequence-dependent conformational preferences of disordered singlestranded RNA." Cell Reports Physical Science 5.11 (2024).
- [3] Plumridge, Alex (2020) Discovering Design Principles to Re-Engineer Functional RNA Elements Using Computational and Microfluidic Approaches.
- [4] Zielinski, Kara A., et al. "Chaotic advection mixer for capturing transient states of diverse biological macromolecular systems with time-resolved smallangle X-ray scattering." IUCrJ 10.3 (2023): 363-375.

# Metabolic Labeling of Mucin-Induced Extracellular Vesicles Isolated from Suspension-Adapted Cell Culture

**CNF Project Number: 2272-14** 

**Principal Investigator(s): Matthew Paszek** 

**User(s): Erik Chow** 

Affiliation(s): Department of Biomedical Engineering, Cornell University

Primary Source(s) of Research Funding: NIH Contact: paszek@cornell.edu, ec829@cornell.edu Primary CNF Tools Used: Malvern NS300 Nanosight

#### **Abstract:**

Extracellular vesicles (EVs) are lipid-membranebound secreted nanoparticles which transport DNA, RNA, and proteins between cells and therefore have great potential as tools for disease diagnosis and treatment. The significance of the glycocalyx in EV biogenesis and function is largely unexplored, and the capacity to effect EV production and properties through rational manipulation of the glycocalyx remains poorly understood. We have previously demonstrated that overexpressing the transmembrane mucin glycoprotein Muc1 in the glycocalyx drives EV secretion in adherent MCF10A cells. Here, we expand these findings to suspension-adapted HEK293F cells and utilize metabolic labeling of inherent EV Muc1 biopolymer coatings as a proofof-concept for engineering EVs with designed molecular payloads.

#### **Summary of Research:**

Extracellular vesicles (EVs) have rapidly garnered attention in biomedical engineering research for their ability to transport DNA, RNA and proteins, making them promising candidates as tools for disease diagnosis and treatment. The glycocalyx is a polymer meshwork of proteins, nucleic acids, and glycans which governs numerous intercellular interactions, but its role in regulating EV biogenesis and function remains poorly understood. It has been previously shown that engineering the glycocalyx via the overexpression of mucin can result in membrane morphologies which are favorable for the formation of EVs1. This report summarizes research from the last year characterizing "mucininduced" EVs isolated from suspension-adapted cell culture and demonstrating the efficacy of bio-orthogonal labeling of EV mucin coatings

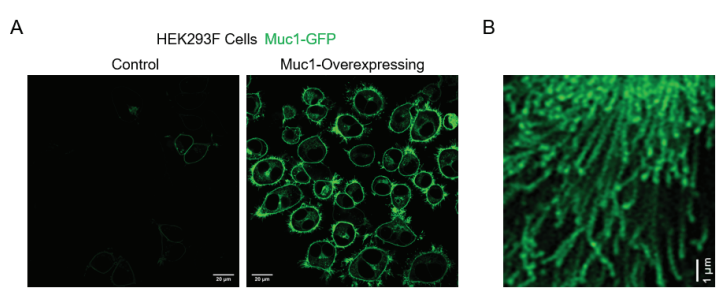


Figure 1: Induced expression of Muc1 biopolymer at the surface of HEK293F cells. A) Confocal fluorescence microscopy images of inducible Muc1-GFP expressed in engineered HEK293F cells. Cells samples were seeded onto poly-L-lysine coated glass-bottom dishes. Non-induced cells (Left) exhibit low leaky expression, while induced cells (Right) exhibit dramatic cell-surface Muc1 expression. Scale bar is 20 μm for both images. B) Pearled cell membrane tubules were observed on the surface of Muc1-overexpressing HEK293F cells. Individual pearls appear to be approximately 200-300 nm in diameter, consistent with structures observed in similarly engineered MCF10A cells. Scale bar is 1 μm.

as a strategy for engineering EV payloads. HEK293F cells were genetically engineered to express tetracycline-inducible Muc1 biopolymer. To induce Muc1 overexpression, cells were treated with 1 ug/mL doxycycline (dox) for 24 h.

Additionally, N-azidoacetylgalactosamine (GalNAz) was added to HEK293F culture media at a final concentration of 50  $\mu$ M at the same time as dox induction. The cells were further incubated at 37  $\Box$ , 5% CO2 for 2 d. EV-containing media was then harvested, and the EVs were isolated by PEG-enrichment according to an existing protocol2. EVs from non-induced cells and EVs from induced cells lacking GalNAz were used as negative controls. EV particle size and concentration were measured by nanoparticle tracking analysis (NTA) using the Malvern NS300 Nanosight.

Expression of cell-surface Muc1 biopolymer in induced HEK293F cells was verified by confocal fluorescence microscopy (Fig 1A). Notably, pearling membrane structures were observed similar to those previously reported on similarly engineered MCF10A cells, suggesting that cell-surface Muc1 could have a similar effect on EV secretion in different cell types (Fig 1B). Indeed, EV secretion was dramatically increased in Muc1-overexpressing HEK293F

cells compared to non-induced control (Figure 2A). Additionally, Muc1 expression resulted in a modest increase in median EV hydrodynamic diameter, consistent with Muc1 biopolymer coatings on the surfaces of mucin-induced EVs (Figure 2B). Metabolic incorporation of GalNAz into the glycans of EV Muc1 biopolymer coatings was confirmed by Western blot. Briefly, mucininduced EVs from HEK293F cells with or without GalNAz incorporation were treated with DBCO-AzDye 568 dye (Click Chemistry Tools), allowing for bio-orthogonal click conjugation of fluorescent reporter to EVs containing GalNAz in their Muc1 surface coatings. Lysates from metabolically labeled and click-conjugated EVs were run on 7% Tris-Acetate SDS-PAGE gels. Western blot confirmed the presence of Muc1 in mucin-induced EV lysates, and further demonstrated successful bio- orthogonal conjugation of fluorescent dye specific to the EVs from HEK293F cells treated with GalNAz (Figure 3).

## **Conclusions and Future Steps:**

These studies reinforce the role of the glycocalyx in EV secretion by demonstrating that the glycocalyx mucin Muc1 drives EV secretion in different cell types. These mucin-induced EVs carry innate mucin biopolymer surface coatings. EV mucin coatings can be further engineered using a combination of endogenous and exogenous modifications to design EV payloads, as demonstrated by the successful bio-orthogonal conjugation of fluorescent reporter molecules to metabolically labeled EVs.

#### **References:**

- [1] Shurer, C. R. et al. (2019). Physical Principles of Membrane Shape Regulation by the Glycocalyx. Cell, 177(7), 1757–1770. https://doi.org/10.1016/j.cell.2019.04.017
- [2] Rider, M. et al. (2016). ExtraPEG: A Polyethylene Glycol-Based Method for Enrichment of Extracellular Vesicles. Sci Rep 6, 23978. https://doi.org/10.1038/ srep23978.

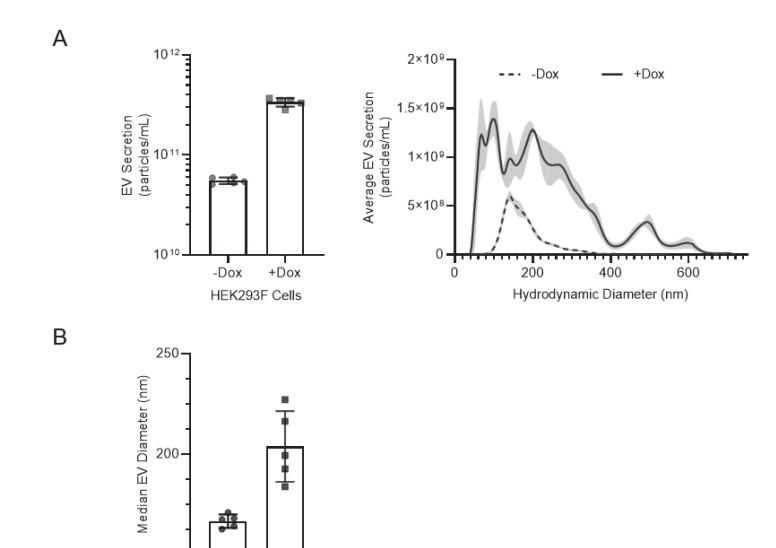


Figure 2: Nanoparticle tracking analysis of mucin-induced EVs isolated from HEK293F cells. A) Comparison of EV secretion from HEK293F cells with low (-Dox) and high (+Dox) Muc1 expression. Bar plot (Left) depicts the average +/- SD from 5 technical replicates.

-Dox

HEK293F Cells

+Dox

Histogram (Right) shows the average secretion +/- SEM from 5 technical replicates for vesicles ranging in size from 0 to 750 nm. B) Comparison of median hydrodynamic diameter (HDD) of EVs from HEK293F cells with low (-Dox) or high (+Dox) Muc1 expression. Bars represent the average +/- SD from 5 technical replicates.

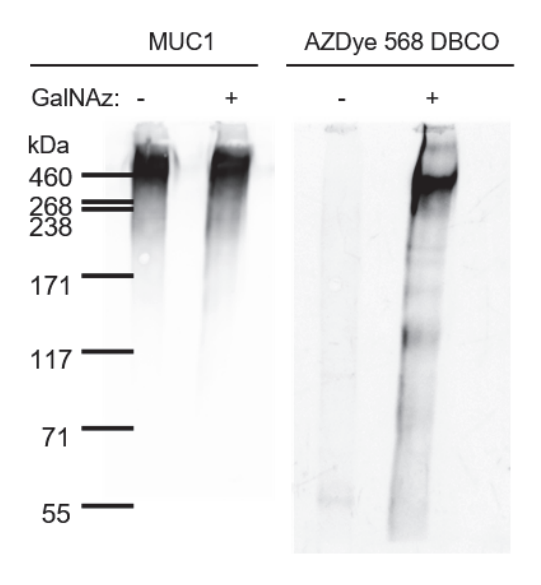


Figure 3: Bio-orthogonal click conjugation of mucin-induced EVs. Western blot detection of Muc1 (Left) and DBCO-AzDye 568 (Right) in lysates of mucin-induced EVs with or without N- azidoacetylgalactosamine (GalNAz) metabolically incorporated into the glycans of EV Muc1 biopolymer coatings.

# **Platform for Live Cells Infrared Chemical Imaging**

**CNF Project Number: 2472-16** 

Principal Investigator(s): Gennady Shvets User(s): Dias Tulegenov, Steven Huang

Affiliation(s): Applied and Engineering Physics, Cornell University

Primary Source(s) of Research Funding: National Cancer Institute of the National Institutes of Health award number R21 CA251052. National Institute of General Medical Sciences of the National Institutes of Health award number R21 GM138947

Contact: gs656@cornell.edu, dt483@cornell.edu, hh633@cornell.edu

Research Group Website: http://shvets.aep.cornell.edu

Primary CNF Tools Used: JEOL 9500, CVC SC4500 Evaporator, Zeiss Ultra Scanning Electron Microscope, Oxford PECVD, PlasmaTherm 740, Glen Resist Strip, DISCO dicing saw, Heidelberg MLA 150, Schott IR inspector

#### **Abstract:**

Our group has been developing infrared spectroscopy and microscopy for live cells analysis by engineering nanostructured antennas on infrared transparent materials and coupling antenna resonances to molecular vibrations. The standard techniques and materials (e.g. e-beam lithography, calcium fluoride substrates, antenna made of gold) used in our device are not scalable due to usage of expensive tools/materials and CMOS incompatible metals. In this report, we focus on replacing our standard substrate, calcium fluoride, used in previous studies with a silicon wafer.

#### **Summary of Research:**

Infrared (IR) spectroscopy is a common non-destructive, label-free technique to identify chemical substances. Previously, we have demonstrated devices (MEIRS [1], 3D-ITS [2], 3D-MEIRS [3]) which are based on coupling plasmonic resonances of nanoantennas to molecular vibrations of chemical components. This allows us to monitor live cell activities such as intracellular activities, cholesterol depletion and cell adhesion. Additionally, by using a mid-IR quantum cascade laser (QCL) light source, our group designed a laser-scanning inverted confocal microscope. The QCL emission is focused on a diffraction-limited spot and scanned across the metasurface through movement of a motorized microscope stage. A liquid-nitrogen-cooled mercury-cadmium-telluride (LN-MCT) mid-IR detector collects modulated reflection from the interaction of the analyte with the metasurface near-fields [4]. Recently we utilized this technique to study metabolic cell differentiation [5]. The vibrational contrast from amide II and lipids (Figure 1) clearly show the high surface sensitivity of our device.

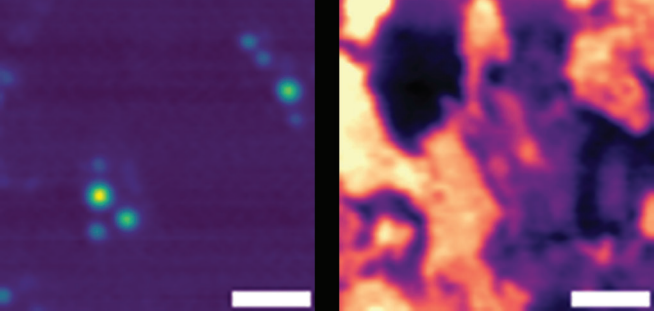


Figure 1: Vibrational contrast of 3T3-L1 at 12C=O ester (left) and amide II (right) bands (scale bar: 40µm).

However, the current substrate (CaF2) is very fragile and poses difficulty if one wants to use larger microplates, typically used for drug discovery studies. This work focuses mostly on replacing CaF2 with a simple silicon wafer with an oxide layer.

The device is made of gold nanoantennas on a doubleside polished 4-inch Si wafer with a silicon dioxide spacer. First, the RCA cleaned silicon wafers were deposited by a 2 µm thick silicon dioxide layer. To pattern nanoantennas, a thin layer of PMMA was spin-coated followed by the e-beam exposure with JEOL9500. After developing, SC4500 evaporator was used to deposit a 5nm Ti adhesion layer followed by 70nm layer of gold to form antennas. Since we use the backside of the substrate to focus IR light, back etched marks located exactly under the metasurface arrays were made by backside alignment using Heidelberg MLA 150 for patterning and PT740 for etching. The last step is to lift-off gold by soaking the wafer/pieces into acetone overnight. Schott IR inspector was used to observe both sides of the wafer, top side having metasurfaces and bottom one having marks (Figure 2).

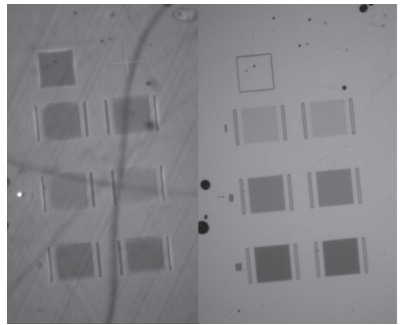
The metasurfaces are then brought to the lab where we culture cancer cells on top of them and acquire images

and spectrum. Figure 3 shows the IR spectra of cells in newly fabricated metasurface. The absorbances magnitudes (vibrational contrast) of amide peaks are comparable to our previous designs, thus making it possible to replace fragile and expensive CaF2 with an unexpensive and easy to make SiO2-on-Si substrates.

#### **Conclusions and Future Steps:**

TWe have demonstrated that our plasmonic metasurface-based devices can also be made with simple Si unlike a standard IR-transparent CaF2 which paves the way for scaling up. We plan to replace expensive e-beam lithography with cheaper and more scalable photolithography (e.g. ASML DUV stepper) for metasurface patterning to large-area microplates. Plus, gold is not a compatible CMOS metal, so we also envision to consider different metals like Ti or Al.

- [1] Huang, S. H. et al. Metasurface-enhanced infrared spectroscopy in multiwell format for real-time assaying of live cells. Lab Chip 23, 2228-2240 (2023).
- [2] Mahalanabish, A. Huang, S. H. Shvets, G. Inverted Transflection Spectroscopy of Live Cells Using Metallic Grating on Elevated Nanopillars. ACS Sens 9 (3), 1218–1226 (2024).
- [3] Mahalanabish, A., Huang, S. H., Tulegenov, D., and Shvets, G. Infrared Spectroscopy of Live Cells Using High-Aspect-Ratio Metal-on-Dielectric Metasurfaces, Nano Lett. 24, 11607–11614 (2024).
- [4] Huang S. H., Shen, PT., Mahalanabish, A., Sartorello, G., Li, J., Liu, X., and Shvets, G. Mid-infrared chemical imaging of living cells enabled by plasmonic metasurfaces, bioRxiv, 2024.09.17.613596.
- [5] Huang, S.H., Tulegenov, D., and Shvets, G. Combining quantum cascade lasers and plasmonic metasurfaces to monitor de novo lipogenesis with vibrational contrast microscopy, Nanophotonics (2025).



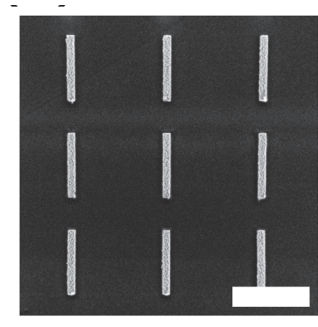


Figure 2: Left and middle figures show the bottom and top side of the wafer, respectively. SEM image of the antennas (right figure, scale bar: 3 µm).

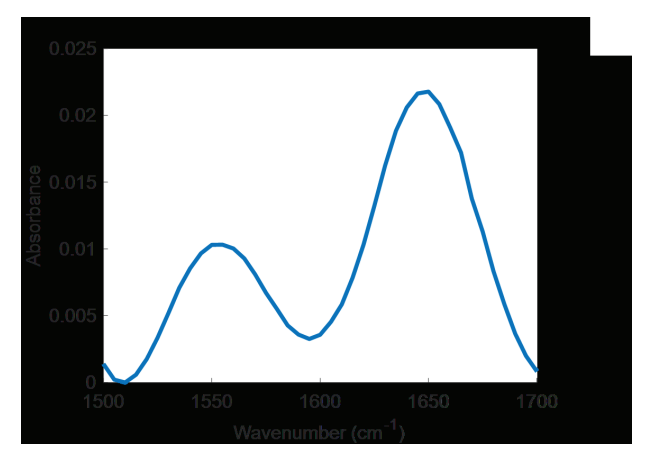


Figure 3: Absorbance spectrum of 3T3-L1 cell measured on the metasurface

# **Circulating Extracellular Vesicles and Physical Stress in ME/CFS**

**CNF Project Number: 2590-17** 

Principal Investigator(s): Maureen R. Hanson

**User(s): Ludovic Giloteaux** 

Affiliation(s): Department of Molecular Biology and Genetics, Cornell University, Ithaca NY

Primary Source(s) of Research Funding: NIH U54 Contact: mrh5@cornell.edu, lg349@cornell.edu

Research Group Website: https://neuroimmune.cornell.edu/research/vesicles-and-signaling/

**Primary CNF Tools Used: Malvern NS300 NanoSight** 

#### **Abstract:**

Myalgic Encephalomyelitis/Chronic Fatigue Syndrome (ME/CFS) is a debilitating and complex multisystem illness that affects millions in the United States. Individuals with ME/CFS suffer from persistent fatigue. cognitive impairment, unrefreshing sleep, and postexertional malaise (PEM), a worsening of symptoms following physical or mental exertion. Growing evidence suggests that extracellular vesicles (EVs), membrane-bound particles released by all cells, play a role in mediating intercellular communication and may contribute to disease pathology. In this project, we used the Malvern NanoSight NS300 Nanoparticle Tracking Analysis (NTA) system to measure concentration of plasma-derived EVs from ME/CFS patients and matched controls across multiple time points surrounding a cardiopulmonary exercise test (CPET). Accurate quantification of EVs is essential not only to assess physiological responses to exercise but also to normalize downstream EV cargo analyses, including surface protein profiling using flow cytometry and RNA-based studies.

## **Summary of Research:**

We used the Malvern NS300 NanoSight NTA instrument to characterize EV populations in plasma samples collected from 28 individuals with ME/CFS and 26 healthy controls. Blood samples were taken before, shortly after, and 24 hours following a CPET. EVs were isolated using standardized protocols to ensure consistency across samples.

Nanoparticle tracking analysis was performed to determine the concentration of EVs in each sample. The resulting data (Figure 1) demonstrate that there is no significant difference in baseline EV concentrations between ME/CFS patients and healthy controls. However, a significant increase in EV concentration was observed in both groups shortly after CPET. This

was followed by a marked decrease in EV levels during the recovery phase (24 hours post- exercise), suggesting dynamic regulation of EV release in response to physical exertion in both healthy and diseased states.

Quantification data from the NTA are also being used to normalize EV input for multiplex surface marker profiling using flow cytometry kits and for RNA cargo analysis. This normalization step is crucial for ensuring meaningful biological comparisons across subjects and time points.

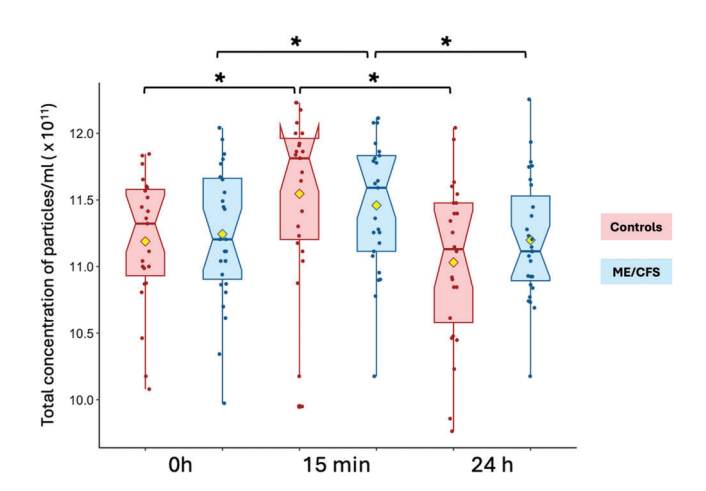


Figure 1: Characterization of extracellular vesicles by Nanoparticle Tracking Analysis. Total concentration of particles per mL of plasma across three time points: before exercise (0h), 15 minutes postexercise, and 24 hours post-exercise.

# **Conclusions and Future Steps:**

Our findings reinforce that EV concentrations increase after exercise and subsequently decline during recovery in both ME/CFS and control groups. This exercise-responsive EV dynamic highlights the utility of NTA for identifying physiologically relevant changes and enabling normalization across sample sets. Ongoing studies are expanding the dataset with additional subjects to improve statistical power. Future work will

focus on integrating surface protein signatures from immunophenotyping using flow cytometry and RNA cargo analysis, allowing us to correlate EV content with exercise response and clinical severity in ME/CFS. These efforts aim to uncover biomarkers of PEM and dysfunctional intercellular signaling in ME/CFS, ultimately improving our understanding of disease mechanisms and therapeutic targets.

#### **References:**

[1] Giloteaux Ludovic and Maureen R. Hanson. Post-exercise changes in mitochondrial DNA of extracellular vesicles in myalgic encephalomyelitis/chronic fatigue syndrome. Poster presentation by L. Giloteaux at the International Society of Extracellular Vesicles (ISEV) 2025 conference held in Vienna, Austria, April 23rd-27th.

# Broadband Electrical Impedance Spectroscopy of Single Cells for Viability Assessment

**CNF Project Number: 2827-19** 

Principal Investigator(s): Alireza Abbaspourrad User(s): Amirhossein Favakeh, Amir Mokhtare, Mohammad Javad Asadi, James C. M. Hwang

Affiliation(s): Department of Food Science, Cornell University, Ithaca 14853, New York, USA; School of Electrical and Computer Engineering, Cornell University, Ithaca, New York 14853, USA; School of Electrical and Computer Engineering, Cornell University, Ithaca, New York 14853, USA

Primary Source(s) of Research Funding: US Army research, development and engineering command Contact: am2964@cornell.edu, ma2297@cornell.edu, jch263@cornell.edu

Primary CNF Tools Used: Heidelberg DWL2000 Mask Writer, ABM Contact Aligner, SUSS MA6 Contact Aligner, Oxford 82 Etcher, SCVC Even-Hour Evaporator

#### **Abstract:**

Single-cell analysis plays an important role in disease diagnosis. However, many characterization methods are labor-intensive, costly, and timeconsuming. Electrical impedance spectroscopy (EIS) offers a label-free, non-invasive method for probing the biophysical characteristics of cells and assessing their viability. Here, we have designed and fabricated a coplanar waveguide (CPW) integrated with microfluidics that can precisely capture a single cell between the gaps of the CPW electrodes. By sweeping the frequency from low (30 kHz) to high (6 GHz) through the cell, we successfully extracted the cellular bilayer electrical properties in real-time monitoring and assessed the cell viability through modeling each layer of the cell with a suggested electrical equivalent circuit.

# **Summary of Research:**

To fabricate the electrode (Figure 1a), first, we spin-coated AZ nLOF 2020 photoresist on a 4-inch fused silica wafer with a thickness of 500 µm. We created the photomask using Heidelberg DWL2000 Mask Writer. Then, we patterned the design using the SUSS MA6 Contact Aligner on the photoresist of the fused silica wafer. After developing with AZ 726 MIF, we removed residual resist by descumming the wafer using the Oxford 82 Etcher. Next, metal layers (20 nm titanium and 500 nm gold) were deposited onto the substrate using an electron beam evaporator. This was followed by a lift-off process to remove unwanted metal and remaining photoresist (Figure 1b).

Photolithography was used to fabricate the microfluidic channel. First, we used SU8-2025 negative photoresist to spin-coat a 20-micron-thick layer onto a silicon wafer. After soft baking, exposure was done using the ABM contact aligner, followed by post-baking and developing with SU8 developer. We then hard-baked the pattern. Afterward, the PDMS was poured over the master mold and placed in the oven at 65°C for 2 hours. Next, we peeled the PDMS off and bonded the microfluidic channel with the CPW intersection gap, ensuring a leak-proof seal. Finally, the CPW input and output were terminated with SMA coaxial connectors (Figure 1c).

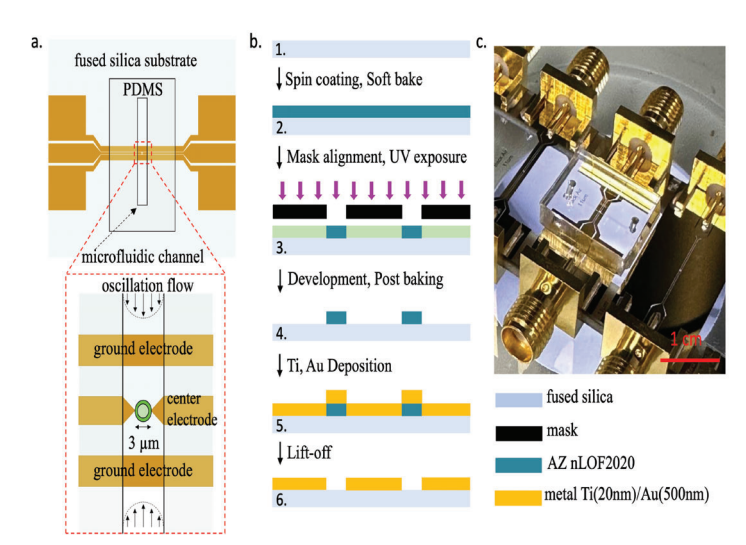


Figure 1: Electrical-impedance microfluidic platform to probe the single-cell biophysical characteristics. (a) Coplanar waveguide (CPW) design. (b) CPW fabrication process. (c) Photograph of the assembled platform.

The platform was connected to the vector network analyzer (VNA), and yeast cells suspended in a low-conductivity 8.5% sucrose solution were injected through the microchannel for final measurements.1 Using dielectrophoresis (DEP), we captured a single cell at 4 MHz and 0 dBm power between

the CPW gap (Figure 2a). With EIS, most of the electric field passes through the cell; 2 therefore, by switching the trapping mode to characterization mode from 30 kHz to 6 GHz and using -18 dBm power, we successfully probed the cell's intracellular properties. Using a two-port measurement, we measured both the membrane and cytoplasm electrical properties, and we assessed cell viability through scattering (S) parameter measurement. The impedance data were then validated by fitting

S-parameters to the proposed equivalent circuit for the cell (Figure 2b) via Advanced Design System (ADS) software.

# Ground electrode Microfluidic Channel $R_{YM}$ $R_{CP}$ $R_{C$

Figure 2: Microwave sensing of a single yeast cell. (a) Trapped single yeast cell between the coplanar waveguide (CPW) electrode gap. (b) Suggested equivalent circuit for each layer of the cell.

## **Conclusions and Future Steps:**

We introduced a high-throughput electrical-impedance microfluidic platform that successfully measures the intracellular electrical properties of single cells. It can distinguish cell viability at high frequencies (3 GHz), where cytoplasm capacitance is dominant. The system enables real-time differentiation between live and dead cells with high accuracy, demonstrating a cytoplasmic capacitance of 3.6 fF for live cells. This platform is fast, accurate, non-invasive, and label-free, enabling real-time monitoring of single cells. It can be used for different electrode configurations and cell types, including mammalian and reproductive cells, for precise single-cell analysis. Future work will focus on EIS measurements of oocytes using this platform to select the best oocyte candidate for assisted reproductive technology (ART) purposes.

- [1] A. Favakeh, A. Mokhtare, M. J. Asadi, J. C. M. Hwang and A. Abbaspourrad, Lab Chip, 2025, 25, 1744–1754.
- [2] J. C. M. Hwang, IEEE Microwave Mag., 2021, 22, 78–87.

# Microfluidic-Based Analysis and Selection of Mammalian Spermatozoa

**CNF Project Number: 2827-19** 

Principal Investigator(s): Alireza Abbaspourrad

User(s): Ali Karimi

Affiliation(s): Department of Food Science, College of Agriculture and Life Sciences, Cornell University

Contact: alireza@cornell.edu, ak2429@cornell.edu Research Group Website: https://abbaspourradlab.com

Primary CNF Tools Used: ABM Mask Aligner

#### **Abstract:**

Successful fertilization depends on navigating the complex, dynamic reproductive tract shaped by geometry and fluid flow. We used microfluidic platforms to study bovine sperm migration under two levels of structural and hydrodynamic complexity. First, we examined rheotactic swimming through tapered microchannel strictures, finding narrower angles (45°) enhance upstream progression while wider angles (90°) impede it. Second, modeling and experiments revealed a novel behavior, rotary rheotaxis, where sperm follow stable, curved upstream paths in outward radial flow. We harnessed this in a microfluidic device combining radial flow and strictures to isolate highly motile sperm from raw semen, advancing sperm-fluidstructure interaction understanding and assisted reproduction technologies.

# **Summary of Research:**

Spermatozoa transverse through and interact with the female reproductive tract (FRT) where they are exposed to a complex microenvironment on their way to the oocyte. Rheotaxis is the reorientation of sperm in a shear flow. We used two level of flow and geometrical complexity on rheotactic sperm navigation: obstructed pathways and radial flows. The microenvironments are fabricated by manufacturing microfluidic devices using conventional soft lithography technique. We used bovine sperm as a model for mammalian sperm.

During their journey in the female reproductive tract (FRT), sperm interact hydrodynamically with complex microstructures formed by the epithelial surfaces of the fallopian tubes. Spatial heterogeneity and muscle contractions cause spatiotemporal geometry changes. Although several studies simulate the FRT using simple

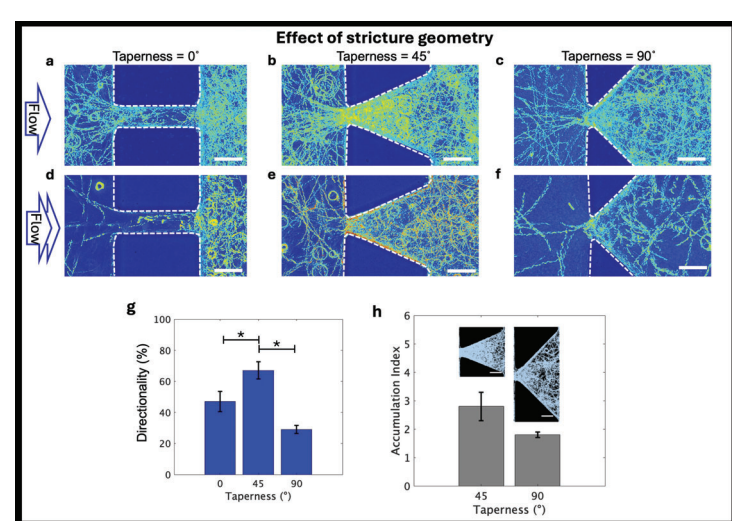


Figure 1: Obstructed pathways mimicking the female reproductive tract, showing sperm trajectories in straight barriers (a, d), tapered barriers with  $\beta = 45^{\circ}$  (b, e) and  $\beta = 90^{\circ}$  (c, f) under average shear rates of 8 and 12 s-1. Trajectories are colorized by grayscale intensity. Scale bar: 100  $\mu$ m. (g) Average directionality across three barrier types under identical flow (p < 0.0001, one-way ANOVA). (h) Accumulation index decreases with increased taper angle from  $\beta = 45^{\circ}$  to  $\beta = 90^{\circ}$ . Overlaid images represent 5-second sperm motion; blue pixels mark sperm presence.

sperm passage channels, none clarify how geometry alterations affect upstream sperm navigation. Previous work showed gate-like behavior of strictures in sperm migration. We systematically studied how barrier geometry affects sperm navigation, mimicking fallopian tube structure (Fig. 1(a–f)). We found that 45° tapered barriers increased navigation by 20% (Fig. 1(g)), while increasing taper to 90° obstructed sperm passage. As shown in Fig. 1(h), accumulation at the barrier apex decreases as taper increases from 45° to 90° under the same shear rate.

We observed that sperm interact and cooperate while passing through the barrier port, forming train-like groups (Fig. 2(a)). This cooperation occurs in three phases: (1) Initial Alignment: temporary orientation at the port entrance due to tapered geometry; (2) Cooperative Train Formation: flagellar synchronization in the high-shear port enhances swimming efficiency; and (3) Dispersal: group disbands upon exiting into the upstream reservoir as shear decreases. To quantify this behavior, we measured inter-sperm distances ( $\Delta r$ ) and

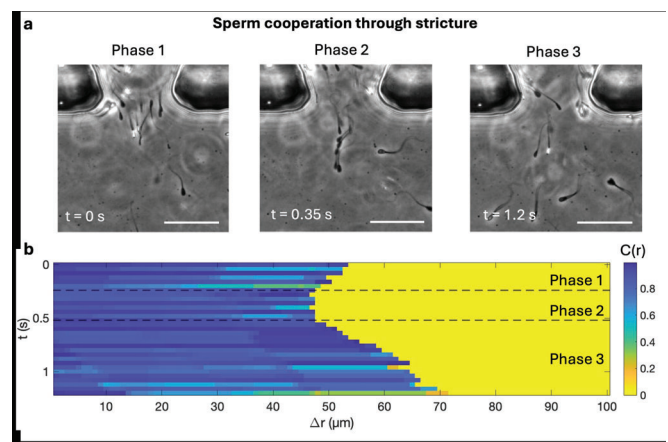


Figure 2: Sperm cooperation in the  $\beta=45^{\circ}$  barrier. (a) Stages: Phase 1—alignment by taper, Phase 2—cooperative train through high-shear port, Phase 3—dispersal upstream. (b) Heatmap of correlation function C(r) over distance and time, showing phase transitions. Color bar: correlation values.

orientation differences ( $\Delta\theta$ ) during a six-sperm event. The correlation function C(r), calculated across distance and time, captures the spatiotemporal dynamics of sperm cooperation (Fig. 2(b)).

We demonstrated that sperm navigate outward radial flow gradients (Fig. 3(a), (b)), showing distinct rheotactic behaviors based on flow rate. At moderate rates, sperm migrated toward the center; at higher rates, they exhibited a rotary rheotaxis, spiraling inward (Fig. 3(c)). This inspired the design of the SUN chip, which combines controlled radial flow with geometric strictures to enhance sperm selection (Fig. 3(e)). Stricture geometry, based on prior work, maximizes upstream navigation while maintaining high shear rates suitable for selecting motile sperm (Fig. 3(f)). Experiments confirmed effective navigation and radial

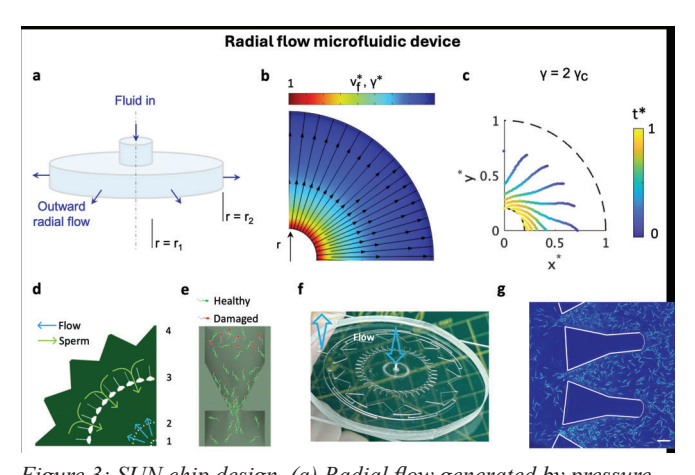


Figure 3: SUN chip design. (a) Radial flow generated by pressure difference between inner  $(r_{\gamma})$  and outer  $(r_{\gamma})$  radii. (b) Normalized velocity  $(v^*)$  decays with  $r_{\gamma}$  streamlines/arrows indicate flow direction. (c) Sperm trajectories at shear rate  $\gamma=2\gamma c$ . Time and dimensions normalized for clarity. (d) Schematic of one-quarter of the chip showing flow direction and regions I–IV. (e) Sperm migration through a stricture. (f) SUN chip image. (g) Sperm navigation in region II.

flow directing sperm toward the origin (Fig. 3(g)). The SUN chip processes raw bull semen at various flow rates, isolating highly motile (>95%) and viable sperm (Fig. 4(a)). Selected sperm showed ~50% higher average path velocity (VAP) than raw semen (Fig. 4(b)). Amplitude of head oscillation (ALH) and beat cross frequency (BCF) increased significantly at most flow rates, indicating more progressive sperm behavior under low to moderate flow (Fig. 4(c)).

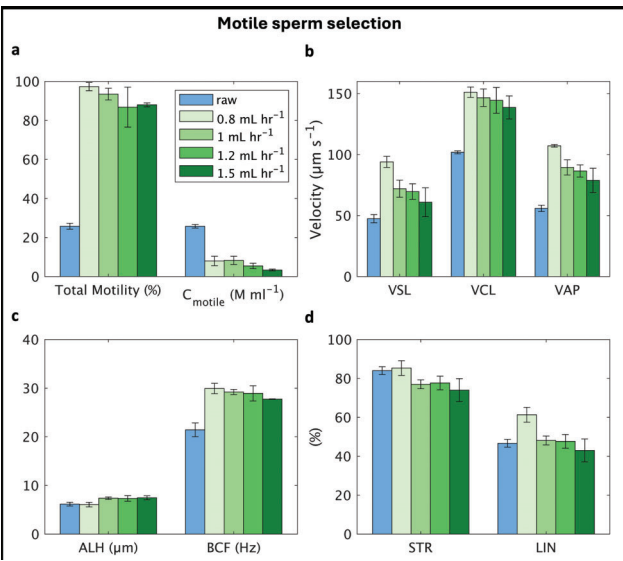


Figure 4: Motility profiles of sperm extracted via SUN chip under flow rates 0.8–1.5 mL/h vs. raw bovine semen. (a) Total motility and motile sperm concentration. (b) VSL, VCL, VAP. (c) ALH and BCF. (d) STR and LIN. SUN chip-processed samples show enhanced motility over raw semen.

## **Conclusions and Future Steps:**

We developed microfluidic devices to study sperm migration in complex environments, focusing on obstructed pathways and radial flow. Our results show that pathway geometry, especially constriction angles, significantly influences rheotactic sperm behavior. Combining geometric strictures with radial flow, we created the SUN chip, which processes  $150\,\mu L$ . This work enhances understanding of microswimmer navigation in dynamic environments and lays groundwork for studying other motile microorganisms. Future efforts should scale processing volume and add automation for clinical use, particularly in IVF. The SUN chip's larger features ease fabrication for mass production, though automation and commercialization challenges remain.

- [1] Suarez, S. S.; Pacey, A. A. Sperm Transport in the Female Reproductive Tract. Hum. Reprod. Update 2005, 12 (1), 23–37.
- [2] Zaferani, M.; Palermo, G. D.; Abbaspourrad, A. Strictures of a Microchannel Impose Fierce Competition to Select for Highly Motile Sperm. Sci. Adv. 2019, 5 (2), eaav2111.
- [3] Karimi, A.; Yaghoobi, M.; Abbaspourrad, A. Geometry of Obstructed Pathway Regulates Upstream Navigational Pattern of Sperm Population. Lab. Chip 2025, 25 (4), 631–643.

# Fabrication of Microchip Devices for Organ-on-a-Chip and Lab- on- a-Chip Applications

**CNF Project Number: 2857-19** 

Principal Investigator(s): Esak (Isaac) Lee

User(s): Wukun Ouyang, Renhao Lu, Yansong Peng

Affiliation(s): Meining School of Biomedical Engineering, Cornell University Primary Source(s) of Research Funding: R01 CA279560; R01 HL165135

Contact: el767@cornell.edu, wo55@cornell.edu, rl839@cornell.edu, yp255@cornell.edu

Research Group Website: https://leelab.bme.cornell.edu/

Primary CNF Tools Used: Heidelberg DWL2000 Mask Writer, ABM Contact Aligner, MVD100, SU-8 hotplate

#### **Abstract:**

Organ-on-a-chip is a microfluidic cell culture platform, integrated circuit (chip) that simulates the activities, mechanics, and physiological response of an entire organ or an organ system. Our lab aims to create organ-on-a-chip devices to study the mechanism of various diseases. In the past year, we mainly focused on three projects: (1) Astrocyte-driven vasoconstriction impairs glymphatic clearance in a human tauopathyon-chip model; (2) Monomeric and oligomeric amyloid-β cause distinct Alzheimer's disease pathophysiological characteristics in astrocytes in human glymphatics-on-chip models; (3) Three-Dimensional Lymphatics-on-a-Chip Distinct, Size-Dependent Nanoparticle Transport Mechanisms in Lymphatic Drug Delivery.

#### **Summary of Research:**

# Project 1: Astrocyte-driven vasoconstriction impairs glymphatic clearance in a human tauopathy-on-chip model [1]

The glymphatic system is a critical pathway for clearing metabolic waste from the brain by mediating cerebrospinal fluid and interstitial fluid exchange. In Alzheimer's disease (AD), tau protein accumulation is strongly associated with impaired glymphatic clearance, yet the underlying mechanism remains poorly defined. In this study, we employed a three-dimensional human glymphatics-on-chip model to investigate fluid transport and mass clearance in a brain-mimetic extracellular matrix containing engineered blood vessels (BV) surrounded by primary astrocytes. We found that phosphorylated tau (p-tau) induced morphological transformation of astrocytes into a hypertrophic, hypercontractile state, leading to astrocyte-mediated vasoconstriction and impaired glymphatic clearance. Notably, p-tau did not affect blood endothelial cells directly, implicating astrocyte-dependent mechanisms in glymphatic deregulation. Pharmacological inhibition of nonmuscle myosin II with blebbistatin reversed astrocytic hypercontractility, restored BV diameters, and rescued glymphatic function. These findings elucidate a glial-specific mechanism of tau-induced glymphatic dysfunction and underscore astrocytic contractility as a promising therapeutic target in AD.

# Project 2: Monomeric and oligomeric amyloid-\$\beta\$ cause distinct Alzheimer's disease pathophysiological characteristics in astrocytes in human glymphatics-on-chip models [2]

Alzheimer's disease (AD) is marked by the aggregation of extracellular amyloid- $\beta$  (A $\beta$ ) and astrocyte dysfunction. For A $\beta$  oligomers or aggregates to be formed, there must be A $\beta$ monomers present; however, the roles of monomeric  $A\beta$  (mA $\beta$ ) and oligomeric A $\beta$  (oA $\beta$ ) in astrocyte pathogenesis are poorly understood. We cultured astrocytes in a brain-mimicking three-dimensional (3D) extracellular matrix and revealed that both mAβ and oAβ caused astrocytic atrophy and hyperreactivity, but showed distinct Ca2+ changes in astrocytes. This 3D culture evolved into a microfluidic glymphatics-onchip model containing astrocytes and endothelial cells with the interstitial fluid (ISF). The glymphatics-on-chip model not only reproduced the astrocytic atrophy, hyper-reactivity, and Ca2+ changes induced by mA $\beta$  and oA $\beta$ , but recapitulated that the components of the dystrophin-associated complex (DAC) and aquaporin-4 (AQP4) were properly maintained by the ISF, and dysregulated by mAβ and oAβ. Collectively, mAβ and oAβ cause distinct AD pathophysiological characteristics in the astrocytes.

### Project 3: Three-Dimensional Lymphatics-on-a-Chip Reveals Distinct, Size- Dependent Nanoparticle Transport Mechanisms in Lymphatic Drug Delivery

Although nanoparticle-based lymphatic drug delivery systems promise better treatment of cancer, infectious disease, and immune disease, their clinical translations are limited by low delivery efficiencies and unclear transport mechanisms. Here, we employed a three-dimensional (3D) lymphatics-on-a-chip featuring an engineered lymphatic vessel (LV) capable of draining interstitial fluids including nanoparticles. We tested lymphatic drainage of different sizes (30, 50, and 70 nm) of PLGA-b-PEG nanoparticles (NPs) using the lymphatics-on-a-chip device. In this study, we discovered that smaller NPs (30 and 50 nm) transported faster than larger NPs (70 nm) through the interstitial space,

as expected, but the smaller NPs were captured by lymphatic endothelial cells (LECs) and accumulated within their cytosol, delaying NP transport into the lymphatic lumen, which was not observed in larger NPs. To examine the mechanisms of sizedependent NP transports, we employed four inhibitors, dynasore, nystatin, amiloride, and adrenomedullin, to selectively block dynamin-, caveolin-, macropinocytosis-mediated endocytosis-, and cell junction-mediated paracellular transport. Inhibiting dynamin using dynasore enhanced the transport of smaller NPs (30 and 50 nm) into the lymphatic lumen, minimizing cytosolic accumulation, but showed no effect on larger NP transport. Interestingly, the inhibition of caveolin by nystatin decreased the lymphatic transport of larger NPs without affecting the smaller NP transport, indicating distinct endocytosis mechanisms used by different sizes of NPs. Macropinocytosis inhibition by amiloride did not change the drainage of all sizes of NPs; however, paracellular transport inhibition by adrenomedullin blocked the lymphatic transport of NPs of all sizes. We further revealed that smaller NPs were captured in the Rab7-positive late-stage lymphatic endosomes to delay their lymphatic drainage, which was reversed by dynamin inhibition, suggesting that Rab7 is a potential target to enhance the lymphatic delivery of smaller NPs. Together, our 3D lymphatics-on-a-chip model unveils sizedependent NP transport mechanisms in lymphatic drug delivery.

- [1] Park R, Peng Y, Yslas AR, Lee E. Astrocyte-driven vasoconstriction impairs glymphatic clearance in a human tauopathy-on-chip model. APL Bioeng. 2025 Jun 16;9(2):026126. doi: 10.1063/5.0261875. PMID: 40530247; PMCID: PMC12173474.
- [2] Yslas AR, Park R, Nishimura N, Lee E. Monomeric and oligomeric amyloid-β cause distinct Alzheimer's disease pathophysiological characteristics in astrocytes in human glymphatics-on-chip models. Lab Chip. 2024 Aug 6;24(16):3826-3839. doi: 10.1039/d4lc00287c. PMID: 39037244; PMCID: PMC11302770.
- [3] Lu R, Lee BJ, Lee E. Three-Dimensional Lymphatics-on-a-Chip Reveals Distinct, Size-Dependent Nanoparticle Transport Mechanisms in Lymphatic Drug Delivery. ACS Biomater Sci Eng. 2024 Sep 9;10(9):5752-5763. doi: 10.1021/acsbiomaterials.4c01005. Epub 2024 Aug 23. PMID: 39176471.

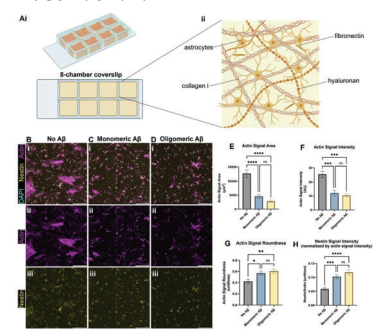


Figure 2: Astrocytic atrophy and reactivity changes in astrocytes exposed to monomeric and oligomeric  $A\beta$ . (A) A schematic of our initial 3D culture of astrocytes. (Ai) Human astrocytes were cultured in 3D ECM in chambers on a glass coverslip, (Aii) with brain-mimicking ECM components including collagen I, hyaluronan, and fibronectin. (B) Immunostaining astrocytes with phalloidin (F-actin staining), anti-nestin antibodies, and DAPI. The astrocytes were exposed to either no  $A\beta$  (B), monomeric (C), or oligomeric  $A\beta$  (D). (E) Changes in actin signal area per cell by monomeric or oligomeric  $A\beta$ . (F) Changes in total actin signal intensity by monomeric or oligomeric  $A\beta$ . (G) Changes in roundness by monomeric or oligomeric  $A\beta$ . (H) Changes in astrocytic reactivity by monomeric or oligomeric  $A\beta$ , as measured by nestin signal intensity relative to actin signal intensity. Scale bars  $(B-D)=200~\mu\text{m}$ . \*(p<0.05), \*\*(p<0.01), \*\*\*\*(p<0.001), and \*\*\*\*\* (p<0.0001) indicate statistical significance. (p<0.001) is significant.

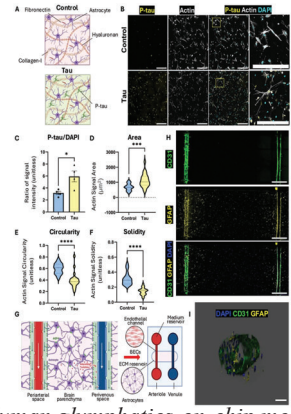


Figure 1: Human glymphatics-on-chip model recapitulates 3D neurovascular architecture with astrocytic reactivity to tau. (a) A schematic representation of the ECM components (astrocytes, fibronectin, collagen I, and hyaluronan) and experimental groups (control, red; tau-treated, green). (b) Immunofluorescence staining of phosphorylated tau (p-tau, yellow), actin (gray), and nuclei (DAPI, cyan) in control and tau-treated astrocytes. Zoomed insets highlight structural changes. (c) Quantification of p-tau signal intensity, normalized to DAPI (N¼ 4). (d) Violin plot showing astrocyte area under control and tau-treated conditions (N¼ 30-40). (e) Violin plot representing astrocyte circularity ( $N\frac{1}{4}$  30–40). (f) Violin plot for astrocyte solidity, showing reduced compactness in tau-treated astrocytes (N<sup>1</sup>/<sub>4</sub> 30–40). (g) A schematic of the in vivo glymphatic system alongside the glymphatics-on-chip platform, depicting the arrangement of astrocytes and blood vessel channels. (h) Immunofluorescence images showing endothelial marker CD31 (green), astrocytic marker GFAP (yellow), and DAPI (blue) within the glymphatics-on-chip platform. (i) A representative, 3D-rendered blood vessel surrounded by astrocytes. Scale bars: 300 lm (b), 1 mm (h), and 100 lm (i). Statistical significance: (p < 0.05), (p < 0.001), and (p < 0.0001).

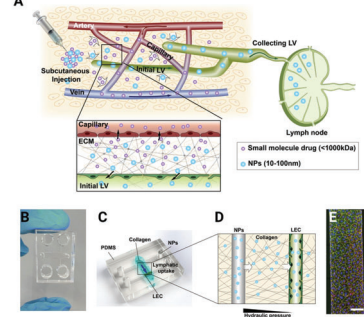


Figure 3: 3D lymphatics-on-a-chip modelto decipher size-dependent nanoparticle (NP) transportinto lymphatic vessels (LVs). (A) Schematic of the NP drug delivery system. Upon subcutaneous injection, water-soluble molecules  $(\stackrel{<}{<} 1000 \text{ kDa})$  are collected by the blood capillary; however, NPs(10-100nm) are preferably drained into the lymphatic vessels via their permeable junctions and reach draining lymph nodes. (B,C) Picture and schematic of the lymphaticson-a-chip model. The collagen bulk (blue) represents the 3D interstitial space, with ECM proteins penetrated by two hollow channels. (D) One of the channels seeded with lymphatic endothelial cells (LECs) forms an engineered LV. The second, cell-free channel allows the introduction of excess fluid to form an interstitial fluid pressure gradient between the acellular and lymphatic channels. Simulating subcutaneous NP injection, excess media, including NPs, are loaded into the acellular channel. NPs transport through the interstitial ECM space, reach the engineered LV, and drain into the LV. Drained and remaining NPs are collected from the 4 circular reservoirs for analysis. (E) Representative image of an engineered LV stained with anti-VE-cadherin (adherens junction, green) antibodies, phalloidin (F-actin, red), and DAPI (nucleus, blue). Scale bar in (E): 100 µm.

# **Nanofabrication of Metallic Barriers for Single Molecule Imaging**

**CNF Project Number: 2927-21** 

Principal Investigator(s): John Brooks Crickard User(s): David Moraga, Ilayda Korkmaz, Mitchell Woodhouse

Affiliation(s): Molecular Biology and Genetics University: Cornell University

Primary Source(s) of Research Funding: NIGMS/Start-UP

Contact: jbc287@cornell.edu, dlm345@cornell.edu, ik353@cornell.edu, mvw25@cornell.edu

Research Group Website: https://blogs.cornell.edu/crickardlab/

Primary CNF Tools Used: Zeiss Supra with Nabity system for lithography, CVC SC4500 Even/Odd hour evaporator

#### **Abstract:**

DNA curtains are a powerful single-molecule technique that can analyze interactions between proteins and DNA in a high-throughput manner. This approach has transformed single-molecule fluorescence microscopy by combining statistical power with the ability to observe proteins moving along individual DNA strands. While other approaches can achieve this statistical power, they generally lack away to control the organization of DNA within a flow cell. We achieve this by nanofabricating chrome barriers onto microscope slides. This allows the alignment of hundreds of individual DNA molecules that can be visualized using total internal reflection fluorescence microscopy (TIRFM). The addition of fluorescently labelled proteins then allows us to monitor specific binding, protein-protein interactions, and the rate of protein movement along DNA. This powerful approach is made possible by equipment maintained in the center for nanofabrication at Cornell.

## **Summary of Research:**

Our research focuses on the application of the DNA curtain technology. We use this approach to perform visual biochemistry approaches and monitor enzymes that function in DNA repair pathways (Figure 1A and Figure 2AB). Our specific work over the last period has focused on how related DNA motor proteins use translocation activity to facilitate the DNA repair process. Below, I will detail two specific projects that have utilized DNA curtains and our specific interactions with the CNF.

# Rdh54 reduces Break induced replication during HR:

Rdh54 is a conserved DNA translocase, known as RAD54B in humans, and is a paralog of Rad54/RAD54L. Rdh54 is semi-redundant with Rad54, but its biological role is still unclear. The dominant

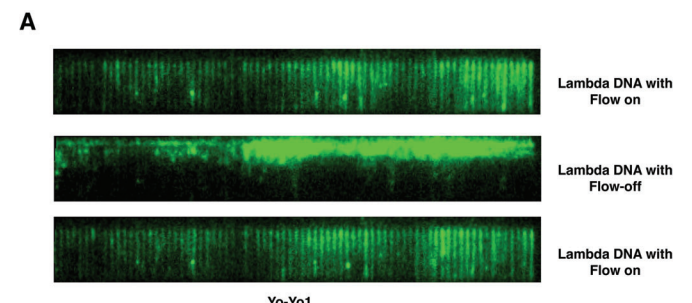


Figure 1: **DNA curtains**(A). Example of DNA curtains. Each green line represents an individual molecule of lambda phage. DNA (48.5 kbp). Flow turns on an off to extend or retract the DNA. The figure is taken from citation E.

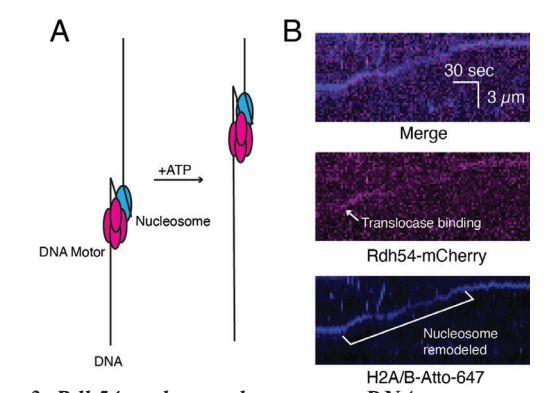


Figure 2: Rdh54 pushes nucleosomes on DNA (A). Cartoon illustrating Rdh54 moving nucleosomes. (B). Direct visualization of Rdh54 moving nucleosomes on DNA. This figure is form citation D.

hypothesis is that Rdh54 reduces Rad51 binding to dsDNA, increasing pools of Rad51 available to promote recombination. However, the role of Rdh54/RAD54B during HR is poorly understood. To improve our knowledge, we investigated the role of phosphorylation in activating Rdh54. Our conclusions from this study are that the effector kinase Rad53 regulates the clustering activity of Rdh54 through a kinase site on the C-terminus of the protein. The kinase activity helps prevent the onset of a mutagenic type of repair, break-induced replication (BIR). This complemented our earlier study, which illustrated that Rdh54 acted to stabilize HR intermediates and provided a novel

mechanism by which Rdh54 improves the fidelity of the strand exchange reaction. Our biochemical studies have been welcomed in the field because of the general challenges in understanding the role of this protein. Studies to understand the biological role of Rdh54 in the template-switching process are ongoing.

#### The activity of Rad54 as a regulator of crossover/ NCO outcomes:

Rad54 is a Snf2 DNA motor protein that remodels DNA and works with Rad51-ssDNA filaments during recombination to catalyze strand exchange. A wealth of information exists on the biochemistry of Rad54 proteins, and we have identified several novel hypomorphic alleles, which allowed us to connect in vitro observations with tangible in vivo phenotypes. Generally, mutations or deletions of Rad54 have resulted in severe sensitivity to genotoxins, which has made developing more refined models for Rad54 function in vivo difficult. We have generated a genetic tool to dissect Rad54's function in all organisms by identifying and developing these hypomorphic alleles. These mutations slow translocation along DNA and in S. cerevisiae cause elevated genetic crossovers between homologous chromosomes during mitotic growth. A key finding from this study is that Rad54 is likely to improve the fidelity of the repair.

#### **Interactions with CNF:**

Our interactions with CNF are limited to the nanofabrication of flow cells, which we use to make flow cells (Figure 3AB). This involved electron beam lithography and chrome deposition to make barriers on the glass slide. These methods require us to train biochemistry and biology students to use the equipment in the cleanroom. These students would not have any interactions with this type of equipment or lithography applications otherwise. This cross-disciplinary training is a part of my research program but is made possible by the CNF.

#### **Conclusions and Future Steps:**

In the future we will continue to train students to make microscope slides.

#### **References:**

[1] Keymakh M\*, Dau J, Ferlez B, Lisby M, Crickard JB. Rdh54 stabilizes Rad51 at displacement loop intermediates to regulate genetic exchange between chromosomes. (2022)



Place Slide nanopattern side up



Place double-sided tape with a strip of paper in between drilled holes



3. Cut our paper strip with a razor blade



4. Fix cover glass to double-sided tape to create flow chamber



5. Melt double sided tape in vacuum oven to seal the flow chamber

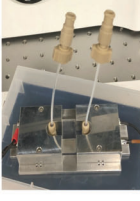


6. Nanoports attached to drilled holes with hot glue

В



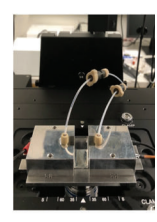
Inlet and Outlet lines
 attached to flow cell
 weell placed in holder



aced in center
I and flow cell



Flow cell is attached to microfluidic lines and flow cell heater placed in universal holder.



4. Front View of flow cell prepared for experiment

Figure 3: Assembly of flow cell for DNA imaging (A). Assembly steps for a flow cell. (B). Assembly of a flow cell on the microscope. This figure is from citation E.

PLOS Genetics PMID:36099310.

- [2] Hu J, Ferlez B, Dau J, and Crickard JB. Rad53 regulates Rdh54 at homologous recombination intermediates. (2023) Nucleic Acids Research PMID: 37850655.
- [3] Sridalla K&\*, Woodhouse M&, Hu J, Scheer J\*, Ferlez B, Crickard JB. The DNA strand opening activity of Rad54 reduces crossover outcomes during homologous recombination. Nucleic Acids Research (2024) PMID: 38828785.
- [4] Woodhouse M, Crickard JB. DNA curtains to visualize chromatin interactions. Methods. 2023 Sep;217:36-42. doi: 10.1016/j.ymeth.2023.07.001. Epub 2023 Jul 10. PubMed PMID: 37437647; PubMed Central PMCID: PMC10529070.
- [5] Crickard JB. Single Molecule Imaging of DNA-Protein Interactions Using DNA Curtains. Methods Mol Biol. 2023;2599:127-139. doi: 10.1007/978-1-0716-2847-8\_10. PubMed PMID: 36427147; PubMed Central PMCID: PMC10082465.

# Fabrication of Microelectrode Arrays for Oxygen Generation to Support Cellular Growth in Implantable Devices

**CNF Project Number: 3066-23** 

Principal Investigator(s): Ahyeon Koh

User(s): Samavi Farnush Bint E Naser, Suk-Heung Song, Jafar Batayneh, Mousa Aldosari

Affiliation(s): Department of Biomedical Engineering, Binghamton University

Primary Source(s) of Research Funding: Advanced Research Projects Agency for Health (ARPA-H), Resilient Extended Automatic Cell Therapies (REACT)

Contact: akoh@binghamton.edu, sbintenaser@binghamton.edu, ssong@binghamton.edu, jbatayneh@binghamton.edu, maldosari@binghamton.edu

Primary CNF Tools Used: AJA Sputterer-1, Oxford 81/82, ABM Contact Aligner, YES Polyimide Bake Oven, P7
Profilometer

#### **Abstract:**

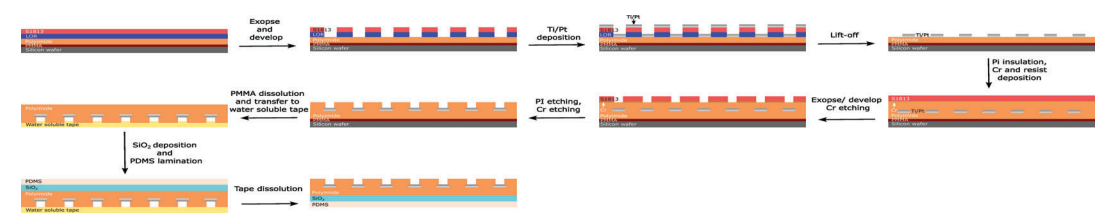
This project aims to develop a microelectrode array for wireless generation of oxygen to support cell culture in implantable, therapeutic devices. To achieve this goal, we have fabricated Platinum (Pt) microelectrodes using tools available at Cornell Nanofabrication Facility (CNF). The microfabricated electrodes are electrochemically coated with Iridium oxide (IrOx) films following transfer to flexible substrates (e.g., PDMS thin films). IrOx catalyzes water splitting, leading to oxygen evolution at a lower potential (~1.2 V) compared to bare Pt (~1.7 V). Based on the oxygen generation performance of the Pt/IrOx electrodes, the microelectrode design will be revised to optimize oxygen generation for cell growth. In future, the Pt/IrOx electrodes will be integrated with NFC chips to allow for wireless operation of the devices.

# **Summary of Research:**

The Ti/Pt microelectrode array is fabricated following the steps in the schematic in Figure 1.1,2 The Si wafers are cleaned and primed with HDMS using the YES vapor process was employed to create the Pt electrodes with LOR 10B as the lift-off resist and Microposit S1813 to define the microelectrode arrays. The AJA sputtering tool was used to deposit 20 nm Ti as the adhesion layer followed by a 100 nm thick Pt layer on the resist bilayer stack. Lift-off was achieved using Remover PG and mild oxygen descum (Oxford 81) post lift-off was used to remove residual resists. Next, a polyimide insulation layer was patterned using photolithography, followed by oxygen etching (Oxford 81) to open active sites on the metal electrodes. A Chromium (Cr) protection layer was used to prevent PI etching from undesired areas, which was removed after the PI etching step, rendering the Tt/Pt microelectrodes ready for the transfer printing step (Figure 2).

Contact profilometry was employed to confirm the final thicknesses of the deposited metal and PI encapsulation layers (Figure 3).

The PMMA layer was dissolved in acetone and water-soluble tapes were used to pick up the electrodes from the wafer (Figure 4A). A 200 nm SiO2 layer was deposited on the electrodes to promote adhesion to final substrates (e.g. PDMS thin films, Figure 4B).



 $Figure\ 1:\ Schematic\ diagram\ for\ fabricating\ Pt\ microelectrodes\ of\ flexible\ support.$ 

Flexible gold wires are used

prime oven at CNF prior to coating with 50 nm PMMA (495 PMMA A5, Kayaku Advanced Materials) and 1.75 µm polyimide (PI 2545, HD microsystems). The lift-off

to connect these microelectrodes to electrochemical stations for targeted compound deposition, such as IrOx, and characterization of oxygen evolution.

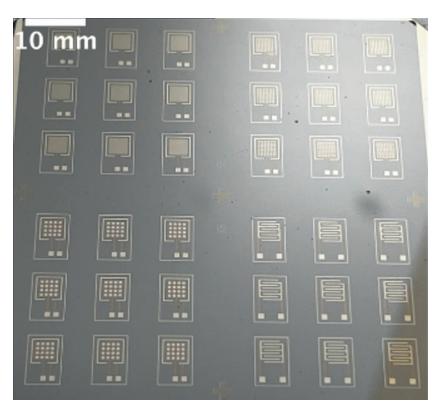


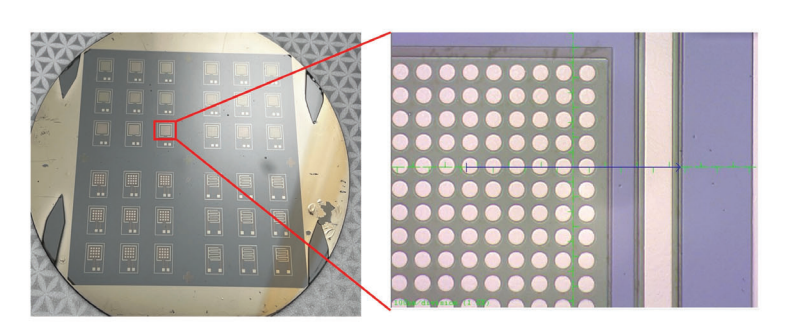
Figure 2: Pt microelectrodes fabricated on polyimide (PI) film supported on Si wafer using sputtering and lift-off.

Images were taken at the end of the fabrication process after PI etching to expose the active electrode areas prior to transfer printing.

#### **Conclusions and Future Steps:**

Based on our preliminary experiments using the microfabricated devices, the designs are being updated to enhance performance. Our group is currently working on evaluating and establishing protocols for the IrOx deposition on microelectrode systems. We are exploring and investigating micro-coil antenna designs to integrate the microelectrodes into a wireless oxygen generation system.

- Brown, M. S., Browne, K., Kirchner, N. & Koh, A. Adhesive-Free, Stretchable, and Permeable Multiplex Wound Care Platform. ACS Sens 7, 1996–2005 (2022).
- [2] Lee, I. et al. Electrocatalytic on-site oxygenation for transplanted cell-based- therapies. Nat Commun 14, 7019 (2023).



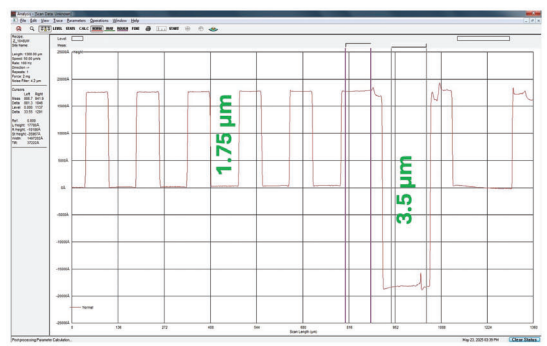
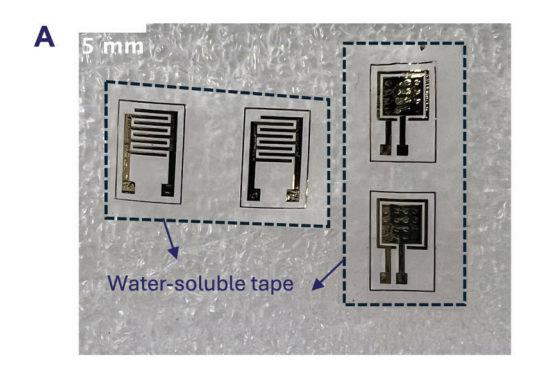


Figure 3: Profilometry performed using the P7 profilometer following the PI etching and Cr removal shows a 1.75  $\mu$ m PI insulation layer patterning the 100  $\mu$ m circular features and a 3.5  $\mu$ m stack of the transferable electrode arrays patterned on the flexible PI supported on Si wafer.



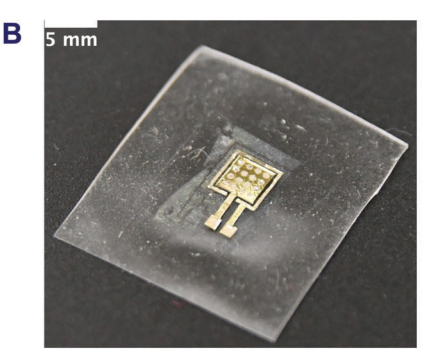


Figure 4: Pt microelectrode arrays (A) after 'pick-up' from the wafer to water-soluble tape and (B) after transferring to PDMS following the SiO2 deposition.

# Generating Dendritic Cell-Mimetic Artificial Antigen Presenting Cell for Optimized T Cell Activation

**CNF Project Number: 3089-23** 

Principal Investigator(s): Negin Majedi

**User(s): Yan Zeng** 

Affiliation(s): Mechanical and Aerospace Engineering, Cornell University

Primary Source(s) of Research Funding: PI startup funds

Contact: fm457@cornell.edu, yz2898@cornell.edu

Primary CNF Tools Used: Hitachi TM3000 SEM, Malvern Nano ZS Zetasizer

#### **Abstract:**

This project aims to develop dendritic cell-mimetic artificial antigen-presenting cells using wrinkled polystyrene particles and chemically treated sunflower pollens to enhance T cell activation. Polystyrene particles are fabricated via solvent evaporation-induced interfacial instability, while pollen shells are prepared through acid-base treatment. Both are coated with polydopamine and conjugated with activation antibodies. Particle size and morphology are characterized using CNF tools: the Zetasizer and Hitachi TM3000 SEM. Future work will focus on improving surface morphology and antibody accessibility to enhance T cell stimulation.

# **Summary of Research:**

Mechanical cues such as substrate stiffness and surface topography are important in regulating T cell activation [1]. This project aims to generate dendritic cell-mimetic artificial antigen presenting cells for optimized T cell activation using synthetic polystyrene particles and natural sunflower pollens respectively. The resulting protruding morphology facilitates the formation of an interaction area between naïve T cells and artificial T cells that mimics the natural immune synapse, which enhances T cell activation and proliferation.

The polystyrene particles are generated using interfacial instability of emulsion droplets during solvent evaporation using the method similar to the method described by Liu et al [2]. Polystyrene emulsion droplets are via homogenization, where the organic phase has polystyrene and 1- hexadecanol dissolved in chloroform, while the continuous phase has sodium dodecyl sulfate and glycerol dissolved in deionized water. The droplet size is optimized by tuning the polymer concentration and homogenization speed. After homogenization, the droplets are solidified under controlled solvent evaporation condition to trigger interfacial instability and form wrinkled surfaces. The solidified wrinkled

polystyrene particles are incubated with deionized water and ethanol respectively to remove residual chloroform, sodium dodecyl sulfate, glycerol, and 1-hexadecanol. Clean particles are coated with polydopamine and conjugated with activation antibodies for T cell activation.

Sunflower pollens are first defatted and then incubated with acid and base respectively to obtain clean, hollow pollen shell for biomedical applications combining the protocols in previous literatures [3], [4]. For the defatting, sunflower pollens are washed subsequently with deionized water, acetone, and cyclohexane. Defatted sunflower pollens are incubated with phosphoric acid and then potassium hydroxide to remove the internal cytoplasmic contents. Clean pollen shells are also coated with polydopamine and then conjugated with activation antibodies for T cell activation.

Both dendritic cell-mimetic artificial antigen presenting cells are co-cultured with native CD4 T cells extracted from mice for three days. After the three-day activation, T cells are stained and examined under flow cytometry to check for activation markers.

Two CNF tools are used to characterize the polystyrene particles and sunflower pollens: Malvern Nano ZS Zetasizer is used for dynamic light scattering measurements to measure the diameter of polystyrene particles generated under different homogenization conditions. Hitachi TM3000 SEM is used to characterize the morphology of polystyrene particles and sunflower pollens.

## **Conclusions and Future Steps:**

For the polystyrene artificial antigen presenting cells, the effect of homogenization speed on particle diameter is shown in Figure 1. The optimal particle diameter is 4-5 microns, which is similar to that of naïve T cells. A lower homogenization speed of 2.8k rpm generates

particles with a diameter of  $1.14~\mu m$ , which is larger compared to those generated at a homogenization speed of 5.2k rpm. To further increase the particle diameter, polymer concentration is further increased. The resulting particles are characterized with instruments outside of CNF and the results are not shown here. The largest polystyrene particles have a diameter of approximately  $4-5~\mu m$ .

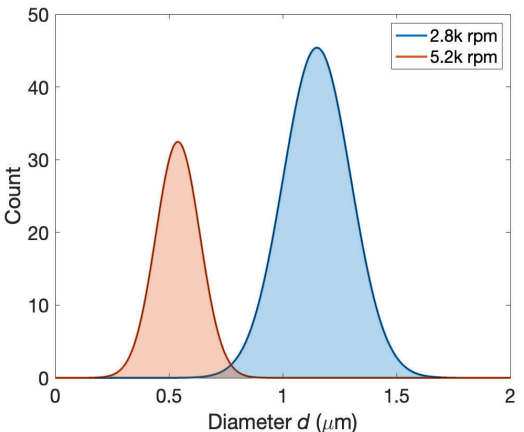


Figure 1: Effect of homogenization speed on polystyrene particle diameter obtained by dynamic light scattering.

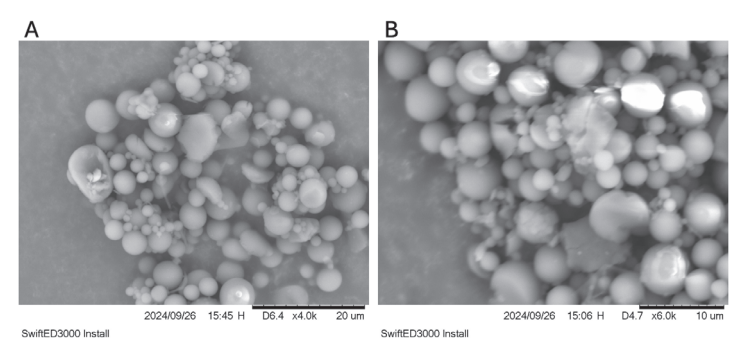


Figure 2: Effect of dialysis against ethanol on polystyrene particle morphology. After (A) 4 days, (B) 6 days dialysis.

The wrinkling is first assumed to happen during the ethanol wash when 1-hexadecanol leaves the droplet, and the ethanol wash is first done via dialysis instead of direct incubation. Figure 2 shows the morphology of polystyrene particles sampled after 4 days and 6 days of dialysis against ethanol respectively. Particles with a diameter of 4-5 um is difficult to image clearly using the tabletop SEM. There's no significant difference in morphology between particles

sampled after 4 days and 6 days of dialysis against ethanol, suggesting that wrinkling is not due to 1-hexadecanol leaving the structure. Alternatively, we assume that wrinkling happens during solidification instead of the ethanol wash, which is later confirmed by Gemini SEM results. For easier imaging, we later switched to Gemini SEM, and the results are not shown here.

The morphology of untreated pollens, acid treated pollens and acid and base treated pollens are shown in Figure 3. Pollens remain intact after acid treatment and base treatment and the spiky features are preserved. Acid treatment opens the apertures on pollen surface, suggesting removal of internal components.

Future work will focus on optimizing the accessibility of conjugated antibodies on pollen shells for more effective activation and increasing the percentage of wrinkled polystyrene particles.

- [1] K. Lei, A. Kurum, and L. Tang, "Mechanical Immunoengineering of T cells for Therapeutic Applications," Acc. Chem. Res., vol. 53, no. 12, pp. 2777–2790, Dec. 2020, doi: 10.1021/acs. accounts.0c00486.
- [2] S. Liu, R. Deng, W. Li, and J. Zhu, "Polymer Microparticles with Controllable Surface Textures Generated through Interfacial Instabilities of Emulsion Droplets," Adv. Funct. Mater., vol. 22, no. 8, pp. 1692–1697, Apr. 2012, doi: 10.1002/adfm.201103018.
- [3] J. M. Ageitos, S. Robla, L. Valverde-Fraga, M. Garcia-Fuentes, and N. Csaba, "Purification of Hollow Sporopollenin Microcapsules from Sunflower and Chamomile Pollen Grains," Polymers, vol. 13, no. 13, Art. no. 13, Jan. 2021, doi: 10.3390/polym13132094.
- [4] [4] P. Gonzalez-Cruz, M. J. Uddin, S. U. Atwe, N. Abidi, and H. S. Gill, "A chemical treatment method for obtaining clean and intact pollen shells of different species," ACS Biomater. Sci. Eng., vol. 4, no. 7, pp. 2319–2329, Jul. 2018, doi: 10.1021/ acsbiomaterials.8b00304.

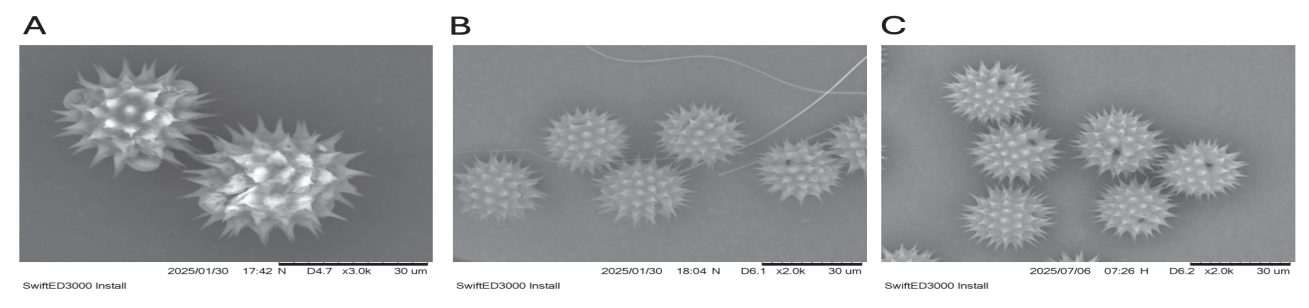


Figure 3: Effect of chemical treatment on pollen morphology. (A) Untreated pollens, (B) Acid treated pollens, (C) Acid and base treated pollens.

# **Exploring Microfabrication Parameters of Template-Based Carbon Nanotube Arrays for Gene Transfer**

**CNF Project Number: 3106-23** 

**Principal Investigator(s): Michael Schrlau** 

User(s): Mujtaba YK Siddiqui

Affiliation(s): Department of Mechanical Engineering, Kate Gleason College of Engineering, Rochester Institute of Technology

Primary Source(s) of Research Funding: : National Institutes of Health R41 GM150320-01 and R43 MH133247-01

Contact: mgseme@rit.edu, mys8553@rit.edu

Research Group Website: https://people.rit.edu/mgseme/Site/Home.html

Primary CNF Tools Used: AJA Ion Mill, PT 740 RIE

#### **Abstract:**

Carbon nanotube (CNT) arrays are a promising new technology which can greatly reduce the costs of novel gene therapies for fighting cancer. It has been fabricated at the Cornell Nanoscale Facility (CNF) using a template-based manufacturing technique. Exploration of the various manufacturing parameters involved in the fabrication would allow for the development of a streamlined and optimized recipe. CNF tools were utilized to study various manufacturing recipes to gain insight into how they affect the surface structure of the device.

#### **Summary of Research:**

Carbon nanotube (CNT) arrays are a promising technology towards developing safer, more economically and technologically accessible method for the transfection of genetic and biomolecular load into cells. Current treatments for diseases like cancer require dangerous and toxic processes. Novel treatments for leukaemia involve gene therapies, the introduction of proteins into white blood cells modifying them to identify cancer. CNT arrays can be used to transfer these proteins into cells. [1–6]

CNT arrays are manufactured from an initial Anodic Aluminum Oxide (AAO) template. Aluminum forms a self-aligned hollow honeycomb-like porous surface when oxidized anodically, allowing AAO to be a commonly used mask for microfabrication at the nanoscale for freestanding nanostructures. Carbon is coated into the pores by means of a chemical vapor deposition (CVD) process. Carbon coated AAO templates are processed at the CNF using the AJA ion mill and PT 740 reactive ion etching (RIE) tools. [7-9] Resulting in a CNT array device with tips of carbon tubes exposed on the surface.

Previous research at the CNF was focused on the scale up of the CNT array manufacturing process. In that work, the manufacturing process was altered by introducing ion milling and employing a larger carrier wafer for producing devices at a larger scale. The work done since that report has built further upon the initial improvements. Exploring alternative starting templates and exploring manufacturing parameters were steps taken towards optimizing the manufacturing process.

The current standard for AAO templates is 13mm diameter disks, this limits the number of cells which can be cultured on each device. A 47 mm diameter template provides a much larger surface area for cell transfer. Figure 1 shows a silicon water affixed with 6 carbon-coated 47mm templates. Fabrication of these devices at the CNF confirmed the capabilities of the current tools and manufacture larger devices. However, the following standard recipe for 13mm did not produce devices with exposed tubes, due to insufficient carbon deposition



Figure 1:Carbon coated 47mm diameter AAO templates on a carrier wafer.

during the CVD step.

Alternative 13mm diameter templates were tested. A template with smaller pore diameters and larger pore density resulted in devices with thicker nanotubes when

undergoing the standard fabrication process. Due to a smaller starting diameter and constant carbon mass flow rate during CVD. Templates of similar properties from other manufacturers were also tested and showed similar surface parameters as standard devices when undergoing the standard fabrication process.

A parametric study of the RIE process time and power was conducted, these parameters are likely to produce the largest impact on the final device. An initial test was conducted to determine the maximum tube height over etch time, as longer etch time is expected to lead to linear growth in exposed tube heights. Followed up by a study of RIE power to determine how increasing power affects tube height. The standard values for RIE etch were 2 hours at 50W power, the experiments covered increasing etch time to 3,4,5 hours and increasing power to 150W and 250W.

Figure 2 and Figure 3 show the results of these experiments; the measurable outputs were the tube height and tube thicknesses of the exposed CNT tips. As shown in the figures, tube heights increase as power and time increase, while tube thickness is maintained until a noticeable drop in thicknesses at larger parameter values. Micrographs showed that at higher powers and etch time the nanotubes tended collapse upon

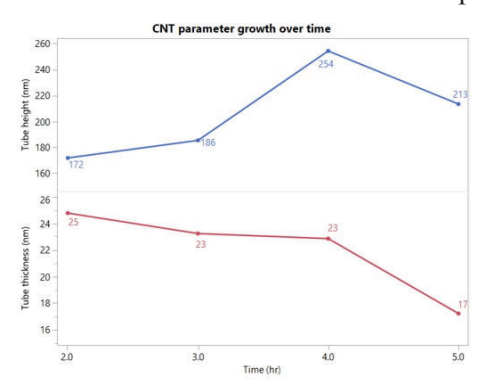


Figure 2: CNT parameters over time.

themselves due to lateral etching thinning them down.

# **Conclusions and Future Steps:**

Exploring alternative starting templates gives an insight into how to scale up the CNT arrays further while making them more useful for researchers and healthcare companies.

Determining the effects of RIE parameters would help establish upper and lower boundaries for future experiments to optimize the process. Next steps would include optimizing the process for 13 mm diameter devices and establishing a working recipe for 47mm diameter AAO templates.

- [1] "Leukemia Treatments." [Online]. Available: https://www.hopkinsmedicine.org/kimmel- cancer-center/cancers-we-treat/blood-bone-marrow-cancers/leukemia-program/current-treatments. [Accessed: 04-Apr-2025].
- [2] "Leukemia: Symptoms, Signs, Causes, Types & Treatment," Cleveland Clinic. [Online]. Available: https://my.clevelandclinic.org/health/diseases/4365-leukemia. [Accessed: 04- Apr-2025].
- [3] "Leukemia Diagnosis and Treatment Mayo Clinic." [Online]. Available: https://www.mayoclinic.org/diseases-conditions/leukemia/diagnosis-treatment/drc- 20374378#. [Accessed: 04-Apr-2025].
- [4] 2019, "Advances in Leukemia Research NCI." [Online]. Available: https://www.cancer.gov/types/leukemia/research. [Accessed: 04-Apr-2025].
- [5] "CAR T Cells: Engineering Immune Cells to Treat Cancer - NCI." [Online]. Available: https://www.cancer.gov/aboutcancer/treatment/research/car-t-cells. [Accessed: 04-Apr-2025].
- [6] "CAR T Cell Therapy," MD Anderson Cancer Center. [Online]. Available: https://www.mdanderson.org/treatment-options/car-t-cell-therapy.html. [Accessed: 04- Apr-2025].
- [7] Li, Z. P., Xu, Z. M., Qu, X. P., Wang, S. B., Peng, J., and Mei, L. H., 2017, "Fabrication of Nanopore and Nanoparticle Arrays with High Aspect Ratio AAO Masks," Nanotechnology, 28(9), p. 095301. https://doi. org/10.1088/1361-6528/aa585c.
- [8] Poinern, G. E. J., Le, X. T., O'Dea, M., Becker, T., and

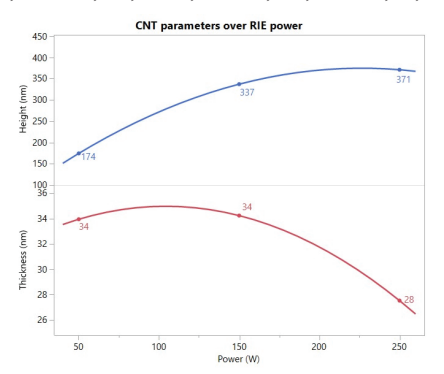


Figure 3: CNT parameters over power.

- Fawcett, D., 2014, "Chemical Synthesis, Characterisation, and Biocompatibility of Nanometre Scale Porous Anodic Aluminium Oxide Membranes for Use as a Cell Culture Substrate for the Vero Cell Line: A Preliminary Study," Biomed Res Int, 2014, p. 238762. https://doi.org/10.1155/2014/238762.
- [9] Golshadi, Masoud, "Carbon Nanotube Arrays for Intracellular Delivery and Biological Applications" (2016). Thesis. Rochester Institute of Technology. Accessed from: https://repository.rit.edu/cgi/viewcontent. cgi?article=10360&context=theses.
- [10] Wiesinger, M., März, J., Kummer, M., Schuler, G., Dörrie, J., Schuler-Thurner, B., and Schaft, N., 2019, "Clinical-Scale Production of CAR-T Cells for the Treatment of Melanoma Patients by mRNA Transfection of a CSPG4-Specific CAR under Full GMP Compliance," Cancers (Basel), 11(8), p. 1198. https://doi.org/10.3390/cancers11081198.

# **Microfluidic Chip Fabrication Using CNF Facilities**

**CNF Project Number: 3193-24** 

Principal Investigator(s): Anne Meyer

**User(s): Danielle Bennett** 

Affiliation(s): University of Rochester

Primary Source(s) of Research Funding: : The Department of Energy, the University of Rochester

Contact: anne@annemeyerlab.org, dbenne15@ur.rochester.edu

Research Group Website: https://sites.google.com/site/annemeyerlab/home

Primary CNF Tools Used: Heidelberg DWL2000, GCA AS200 i-line Stepper, Oxford PECVD, Oxford 81 RIE

#### **Abstract:**

This project aimed to enable long-term fluorescence microscopy imaging of Shewanella oneidensis interactions with CdSe quantum dots by immobilizing motile bacteria physically within a channel instead of through chemical binding. To achieve this, we designed a custom "mother machine" microfluidic device composed of parallel microchannels branching from a main fluid channel. These side channels were aimed to be dimensionally matched to the diameter of individual bacteria, allowing for their physical confinement while maintaining media exchange, thus facilitating continuous observation over time. Fabrication of the device required high-resolution soft lithography using

polydimethylsiloxane (PDMS) cast from a silicon mold. The Cornell NanoScale Science and Technology Facility (CNF) was essential for the creation of this master silicon mold. We used the Heidelberg DWL2000 laser writer for mask patterning, followed by photolithographic processing with the GCA AS200 i-line Stepper. Feature development and refinement were carried out using the Oxford PECVD for surface passivation and the Oxford 81 RIE system for precise etching. This platform aimed to allow us to resolve real-time nanoscale interactions

between fluorescent nanoparticles and live bacteria, offering new insight into quantum dot— microbe dynamics. The machinery at the CNF facility was required to obtain the small diameter (below  $0.7~\mu m$ ) of the channel features, which was not attainable using our equipment or any commercial equipment.

# Summary of Research:

This microfluidics chip was designed to address the challenge of imaging interactions between motile Shewanella oneidensis bacteria 1,2 and CdSe quantum dots, which are used in our broader research on nanoparticle-based catalysis. Traditional imaging platforms require timescales too long to monitor these highly motile cells over time, so we engineered an ultraminiaturized "mother machine" to trap individual bacteria in channels that are significantly smaller than those used in previous designs3—pushing the limits of soft lithography resolution.

The design of the microfluidic chip centered on creating

a high-resolution "mother machine" with sub-micron precision, featuring narrow side channels approximately 0.7 µm wide branching off a main flow channel approximately 25 µm wide. The chip was constructed from PDMS cast on a silicon mold, with SU-8 photoresist features forming the mold's surface relief. The layout was designed in KLayout software with extensive support from CNF staff, particularly Garry Bordonaro and Aaron Windsor, who provided critical guidance on optimizing the design for photolithography and transitioning from square to rounded channel geometries. This design adjustment,

made between Figure 1 and Figure 2, significantly improved fluid dynamics by reducing backflow and enhancing media exchange across the confined bacteria. Fabrication at CNF involved multiple cleanroom steps, including photomask writing with the Heidelberg DWL2000, mask alignment and exposure using the GCA AS200 i-line Stepper, and multilayer etching using the Oxford 81 RIE system. Due to the chip's extremely fine features, the etch process required a two-step

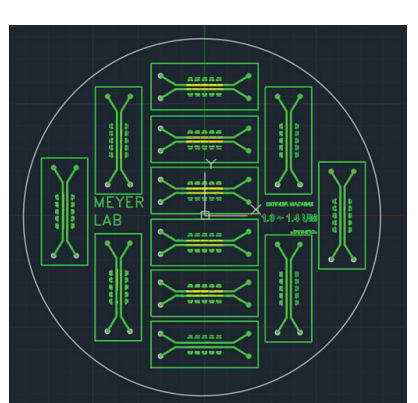


Figure 1: The initial mother machine chip design featuring sharp rectangular channels.

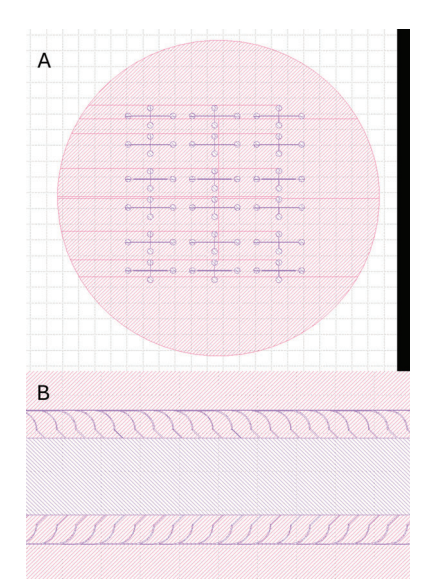


Figure 2: The mother machine design revised with the assistance of CNF staff featuring curved channels. Part A shows the full chip design and part B shows a closer view of the main channel and branching channels.

approach developed with the help of Jeremy Clark, who also provided expertise on the Oxford PECVD system for wafer preparation. Extensive cleanroom training and tool-specific instruction were essential to successfully executing this complex fabrication process.

To test the chip, PDMS was cast onto the fabricated silicon master and cured to form the microfluidic structure, which was then plasma treated and bonded to a glass coverslip to seal the channels. Fluidic testing involved introducing S. oneidensis cells into the device using a syringe pump to establish controlled flow through the microchannels. This functional testing revealed two key issues: first, the side channels were not sufficiently narrow to trap individual bacteria effectively, as shown in Figure 3; and second, leakage occurred at higher flow rates, suggesting inadequate bonding or minor defects at the PDMS–glass interface. These outcomes highlighted

Figure 3: An image of the PDMS structure fabricated using the mask. Bacteria can be observed outside of the microchannels due to leakage at higher flow rates, and the side channels were slightly too large to trap the bacteria.

the need for tighter feature tolerances and improved sealing, prompting a redesign of the channel dimensions and further optimization of the fabrication protocol.

#### **Conclusions and Future Steps:**

Although the initial version of the microfluidic chip did not fully meet the functional requirements for long-term bacterial confinement, the fabrication process validated several critical aspects of the design and demonstrated the capabilities of CNF's advanced lithographic and etching tools. The pattern transfer from the KLayout design to the silicon mold using the Heidelberg DWL2000 and GCA AS200 i-line Stepper was highly successful, yielding clean and reproducible features at both the sub-micron and tens-of-micron scale. The twostep etching process developed with guidance from CNF staff, particularly Jeremy Clark, allowed for precise control over feature depths, which is essential for the multi-scale structure of the chip. While the final PDMS device exhibited some leakage at higher flow rates and did not achieve full bacterial trapping due to overly large side channels, these outcomes provided direct feedback that will inform future improvements.

The ability to prototype a custom-designed, high-resolution microfluidic device at this level would not have been possible without access to CNF's advanced photolithography and etching infrastructure, nor without the expert technical support provided throughout the process. This project has laid the groundwork for developing a next-generation mother machine capable of precisely trapping S. oneidensis for extended imaging of nanoparticle–microbe interactions. Moving forward, refined designs will incorporate narrower channel geometries and optimized bonding techniques to address current limitations. At this point no publications have been drafted.

- [1] Edwards, E. H.; Jelusic, J.; Kosko, R. M.; McClelland, K. P.; Ngarnim, S. S.; Chiang, W.; Lampa-Pastirk, S.; Krauss, T. D.; Bren, K. L. Shewanella Oneidensis MR-1 Respires CdSe Quantum Dots for Photocatalytic Hydrogen Evolution. PNAS 2023, 120, 17. https://doi.org/10.1073/pnas.
- [2] Bennett, D. T.; Meyer, A. S. Robust Measurement of Microbial Reduction of Graphene Oxide Nanoparticles Using Image Analysis. Appl Environ Microbiol 2025, 0 (0), 9–11. https://doi.org/10.1128/aem.00360-25.
- [3] Yang, D.; Jennings, A. D.; Borrego, E.; Retterer, S. T.; Männik, J. Analysis of Factors Limiting Bacterial Growth in PDMS Mother Machine Devices. Front Microbiol 2018, 9 (MAY), 1–12. https://doi.org/10.3389/fmicb.2018.00871.

# **Microfluidic Systems for Studying Bacteria Mechanobiology**

**CNF Project Number: 3229-24** 

Principal Investigator(s): Christopher J. Hernandez

**User(s): Jay VanDelden** 

Affiliation(s): UC San Francisco, UC Berkeley

Primary Source(s) of Research Funding: : NSF 2135586, 2125491 Contact: christopher.hernandez@ucsf.edu, jvd@eigenphase.com

Research Group Website: hernandezresearch.com

Primary CNF Tools Used: AJA Sputter Deposition, 2 Gamma tool, ASML tool, Oxford 81 or Oxford 82 PT770,

Oxford, 100, Versalaser

#### **Abstract:**

In this project we seek to understand the biomechanical properties of individual bacteria as well as bacterial mechanobiology (the response of living bacteria to mechanical stimuli). We have four goals in this project:

1) to determine mechanical properties of bacterial cell envelope of various species; 2) to understand how to embed and maintain viable bacteria within rigid materials, the so-called "engineered living material." 3) to utilize mechanical stimuli to promote biomineralization of ureolytic bacteria; and 4) to understand how bacteria grow into constricted space.

### **Summary of Research:**

Currently, we are working on to demonstrate that mechanical stimuli can be used to promote biomineralization of ureolytic bacteria by using microfluidic device and genetically modifying a bacterial strain to link mechanosensitive gene to biomineralization gene. Additionally, we are working on to analyze how S. aureus grow and devide in a constricted space using the microfluidic devices manufactured at CNF. Since the inception of this project number we have been manufacturing devices with the help of Jay VanDelden (Eignphase).

# **Silicon Nitride Cantilevers for Muscle Myofibril Force Measurements**

**CNF Project Number: 3236-52** 

Principal Investigator(s): Walter Herzog

**User(s): Andrew Sawatsky** 

Affiliation(s): Faculty of Kinesiology, University of Calgary, Calgary, Canada Primary Source(s) of Research Funding: : Canadian Institutes of Health Research

Contact: wherzog@ucalgary.ca, ajsawats@ucalgary.ca

Research Group Website: https://kinesiology.ucalgary.ca/research/labs-and-centres/human-performance-lab

Primary CNF Tools Used: GCA 5X Stepper, SUSS MA6-BA6 Contact Aligner, Photolith spinners, Oxford 81 ion etcher, Reynolds Tech KOH Hood, Heidelberg DWL2000, MRL E4 LPCVD CMOS Nitride

#### **Abstract:**

Measurement of nano-Newton forces produced by individual sarcomeres and isolated myofibrils is possible using custom silicon-nitride cantilever pairs [1]. Advanced imaging techniques, including phasecontrast and immunofluorescent microscopy, allow for the correlation of visible physiological features with mechanical properties – at the level of the sarcomere. Recent advances in our lab have enabled, for the first time, fluorescent labelling of the giant spring-like protein titin without compromising mechanical properties of the sarcomere. Thus, the purpose of this study was to 1: identify the position of select antibody labels on titin during sarcomere elongation and 2: confirm if eccentric calcium-activation causes titin-actin binding, as has been widely suggested [2]. Using myofibrils isolated from rabbit psoas, we performed labelling of titin using N2A (anti-TTN-N2A, Myomedix, Germany) and F146.9 (anti-TTN-F146.9B9, Myomedix, Germany) primary antibodies followed by AlexaFluor488 (A32723 ThermoFischer Scientific, Illinois, United States) and AlexaFluor647 (A21449. A21244, ThermoFischer Scientific, Illinois, United States) secondary fluorophore conjugated antibodies. Chosen N2A and F146.9 primary antibodies flank titin's extensible PEVK segment, which is primarily responsible for titin elongation at physiological sarcomere lengths. Simultaneous measurement of the length of titin's PEVK segment during sarcomere elongation showed similar behavior to non-simultaneous previous experiments [3]. Post eccentric activation, measured PEVK segments were ~50nm longer than isometrically activated controls, suggesting increased force on titin caused by a proximal binding site. In all experiments tested, antibody labels had no effect on mechanical force production compared to protocol-matched unlabelled controls. In conclusion, for the first time, we labelled the sarcomeric protein titin without compromising mechanical function of the sarcomere. This novel labelling system allowed us to confirm both the behavior of titin's PEVK segment during sarcomeric extension and show evidence for titin-actin binding caused by eccentric activation.

#### **Summary of Research:**

Imaging of isolated myofibrils was performed using an inverted Olympus IX83 microscope, and analysis performed using CellSens® Dimensions software. Both phase contrast (PC) and fluorescent channels (AF488, AF647) were collected simultaneously, allowing for the identification of Z-lines (PC), M-lines (PC), TTN-N2A (AF488), and TTN-F146.9 (AF647) within myofibrils (Figure 1). Isolated myofibrils were attached to a glass needle and custom silicon nitride cantilever pairs. Stretching protocols were performed using the glass needle, moved using a piezoelectric motor. Force measurements were performed using optically measured

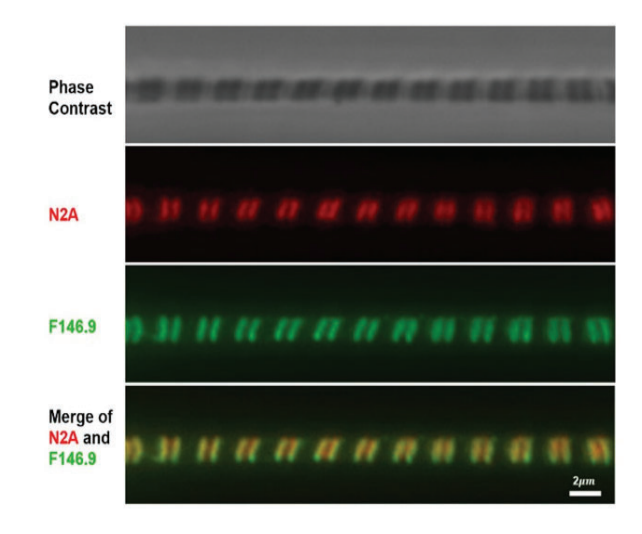


Figure 1: Isolated rabbit psoas myofibril visualized in phase contrast and fluorescent channels. Titin N2A labels are visualized in red (AlexaFluor647); Titin F146.9 labels are visualized in green (AlexaFluor 488). PEVK lengths were measured as the distance between Titin N2A and Titin F146.9 label centroids.

displacement of custom silicon-nitride cantilever pairs with known spring constants.

The introduction of titin labels (N2A and F146.9) did not compromise passive force production during passive sarcomere extension (Figure 2). Since titin is primarily, if not completely, responsible for the production of passive force during sarcomere extension, we concluded that our labelling system did not affect the mechanical behaviour of titin.

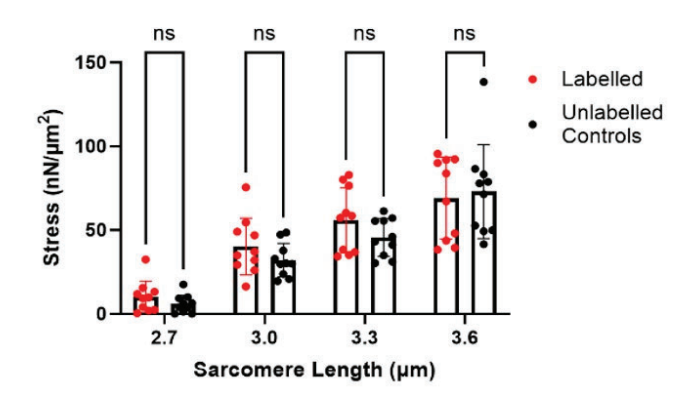


Figure 2: Passive stress production of Labelled myofibrils (n=10) is identical to unlabeled controls (n=10), (2-way ANOVA with Tukey's multiple comparisons test,  $\pm SD$ )

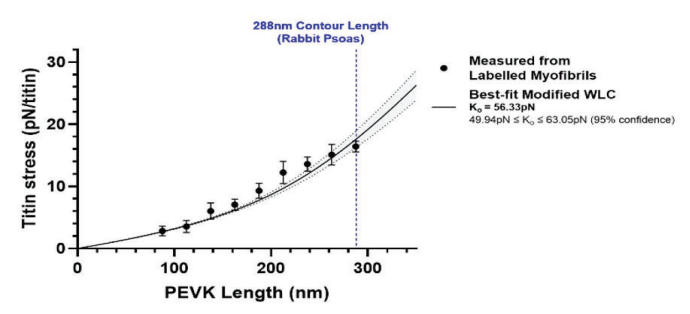


Figure 3: Stress-length relationship of titin's PEVK during passive extension. Data points are means of 25nm length bins, each containing  $\geq$  11 sarcomeres  $\pm$  SEM. Data fit using a modified WLC model showing 95% confidence interval.

We captured the passive extension of titin's PEVK segment in labelled myofibrils (n=10, Figure 3). Extension of the PEVK segment was well modeled using the existent modified worm-like chain model for titin's PEVK region [3]. Thus, we found that in-situ extension of titin's PEVK, when titin is in its natural configuration inside a sarcomere, largely reproduces previously shown extension of isolated titin molecules.

It has been long theorized that titin-actin binding may occur during eccentric activation of muscle, thus leading to 'over-extension' of titin, and sustained increased force production termed residual force enhancement [2]. In 26 sarcomeres, from n=7 myofibrils, we measured the length

of titin's PEVK post eccentric stretch. Titin's PEVK was significantly longer post-eccentric stretch compared to isometrically activated controls, thus providing strong evidence for titin-actin binding proximal to the PEVK region (Figure 4).

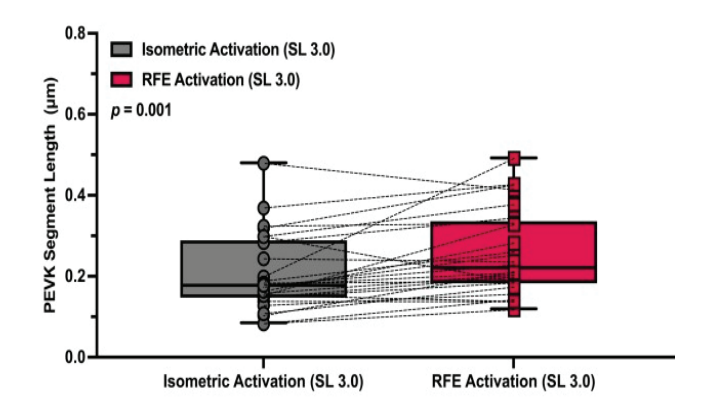


Figure 4: Titin's PEVK is significantly longer post-eccentric activation (RFE activation) compared to isometric controls (Isometric activation) (p =0.001, paired T-test).

#### **Conclusions and Future Steps:**

In conclusion, simultaneous measurement of forces produced by single sarcomeres and immunofluorescent imaging of titin allowed for the identification of insitu behavior of the titin filament and showed strong evidence for titin-actin interactions during eccentric sarcomere activation. These findings support future advanced microscopy for subcellular biomechanics.

- [1] M. E. Fauver, et al. IEEE Trans Biomed Eng 45(7):891-898, 1998.
- [2] Walter Herzog. J Exp Biol 15; 217(16): 2825–2833, 2014.
- [3] W. Linke et al. PNAS 95(14): 8052-8057, 1998.